Identification and control of diffusive systems applied to charge trapping and thermal space sensors

María Teresa Atienza García

Identification and Control of Diffusive Systems Applied to Charge Trapping and Thermal Space Sensors

Dissertation presented as a *compendium of publications*
in partial fulfillment of the requirements for the degree of
Doctor in Electronic Engineering

María Teresa Atienza García

Co-advisors: Dr. Manuel Domínguez Pumar
Dr. Vicente Jiménez Serres

December 2017

Electronic Engineering Department

A mis padres

Acknowledgments

Me gustaría mostrar mi más sincero agradecimiento a todas las personas que de una forma u otra han contribuido a la realización de esta tesis.

En primer lugar, a mis directores de tesis, Manuel Domínguez Pumar y Vicente Jiménez Serres, siempre dispuestos a ayudarme en todos estos años. Sobre todo agradecer a Manuel el ayudarme a encauzar todo este trabajo en forma de tesis, ya que hasta este momento, en el que veo el final, no tenía del todo claro que esto fuera posible. Una mención especial se merece Luis Castañer, a quien le debo haber formado parte del equipo de Marte. Considero que trabajar con él ha sido una experiencia muy enriquecedora, y por ello le doy las gracias.

Quiero dar las gracias al departamento de Instrumentación Avanzada del Centro de Astrobiología (CSIC-INTA) de Madrid, por la oportunidad que me dieron de trabajar con ellos. En especial a Josefina Torres, Sara Carretero, Sara Navarro, Mercedes Marín y Javier Gómez Elvira. Realmente conseguisteis que las horas frente al túnel de viento se me pasaran volando!

Gracias también a mis compañeros del día a día: A Gema López (gracias por enseñarme a trabajar en la sala blanca!), Sergi Gorreta, Lukasz Kowalski, Chenna Bheesayagari, Eric Calle, Chen Jin, Guillermo Gerling y al resto de mis colegas del D213. También agradecer su ayuda a los técnicos Santi Pérez y Miguel García. Gracias a todos por los buenos momentos que he pasado con vosotros!

Gracias a Carmen, Elvira, Irantzu, Itxaso, Iván y Goizargi. Vuestras visitas a Barcelona han hecho que el estar todo este tiempo fuera de casa fuera mucho más llevadero. Y sobre todo, gracias a Emma, que aunque ya no esté por aqui, ha sido mucho tiempo aguantandome fuera del trabajo. Gracias también a mis antiguos compañeros de la UPV/EHU, sobre todo a Joana Pelaz, con quien compartí tan buenos ratos en Torrejón de Ardoz y a Virginia Rubio. Muchísimas gracias!

Dar también las gracias a mi hermano Roberto y a Laura, y en especial, quiero dar las gracias a mis padres, que siempre me han animado a que me dedicara a lo que más me gustaba. Estoy segura de que sin ellos esto no hubiera sido posible.

Y por último, y no por ello menos importante, gracias a Carlos, por tu apoyo incondicional y tu paciencia, que es mucha. Pero sobre todo, gracias por estar siempre ahí.

Abstract

The work underlying this Thesis, has contributed to the main study and characterization of diffusive systems. The research work has been focused on the analysis of two kind of systems. On the one hand, the dynamics of thermal anemometers has been deeply studied. These sensors detect the wind velocity by measuring the power dissipated of a heated element due to forced convection. The thermal dynamics of different sensor structures have been analyzed and modeled during the Thesis work. On the other hand, we have dealt with microelectromechanical systems (MEMS). The dynamics of charge trapped in the dielectric layer of these systems has also been studied. It is know, that this undesired effect has been associated to diffusion phenomena.

In this Thesis a characterization method based on the technique of Diffusive Representation (DR), for linear and nonlinear time-varying diffusive systems, is presented. This technique allows to describe a system with an arbitrary order state-space model in the frequency domain. The changes in the dynamics of a system over time may come as a result of the own actuation over the device or as a result of an external disturbance. In the wind sensor case, the time variation of the model comes from the wind, which is an external disturbance, whereas in the MEMS case, changes in the actuation voltage generate time-variation in the model.

The state-space models obtained from DR characterization have proven to be able to reproduce and predict the behaviour of the devices under arbitrary excitations. Specifically, in the case of wind sensors, the thermal dynamics of these sensors, under constant temperature operation, has been predicted for different wind velocities using Sliding Mode Controllers. As it has been observed, these controllers also help to understand how the time response of a system, under closed loop, can be accelerated beyond the natural limit imposed by its own thermal circuit if the thermal filter associated to the sensor structure has only one significative time constant.

The experimental corroboration of the thermal analysis is presented with various prototypes of wind sensors for Mars atmosphere. On one side, the time-varying thermal dynamics models of two different prototypes of a spherical 3-dimensional wind sensor, developed by the Micro and Nano Technologies group of the UPC, have been obtained. On the other side, the engineering model prototype of the wind sensor of the REMS (Rover Environmental Monitoring Station) instrument that it is currently on board the Curiosity rover in Mars has been characterized.

For the characterization of the dynamics of the parasitic charge trapped in the dielectric layer of a MEMS device, the experimental validation is obtained through quasi-differential capacitance

measurements of a two-parallel plate structure contactless capacitive MEMS.

The only source of knowledge
is experience.

Albert Einstein

Contents

Chapter 1

Introduction

1.1 Framework

The work underlying this Thesis, has contributed to the main study and modeling of diffusive systems. The concept of diffusion can be defined as the physical time-dependant process that causes the 'spread out' of a magnitude from a point or location with high concentration of that magnitude to an area of low concentration.

Along the research work, the time-varying dynamics of some types of diffusive systems have been studied. On the one hand, we have thermal systems. For the study of these systems, we have taken into consideration the thermal dynamics of different prototypes of wind anemometers. To this effect, two main types of wind sensors have been thermally characterized: different prototypes of a spherical 3-dimensional wind sensor, recently developed by the Micro and Nano Technologies group of the Universitat Politècnica de Catalunya (UPC) and the engineering model prototype of the wind sensor of the REMS (Rover Environmental Monitoring Station) instrument, which is currently in Mars on board the Curiosity rover [1]. The working mode of these sensors is Constant Temperature Anemometry (CTA). Under this mode of operation, the temperature in the heating elements of the sensor are forced to be constant and the power required at every element to keep constant the temperature is the output signal of the sensor, from which the wind velocity is inferred [2]. In section 2.1, a full detailed description of these sensors is provided as well as the description of other wind sensors used in the several missions to Mars that have included equipment to measure the wind.

The dynamics of a wind sensor is considered time-varying due to the fact that the changes in the wind velocity generate changes is the system dynamics. Thermal characterization of the dynamics as a function of the wind applied is then of relevance for the design and operation of these type of sensors. Future missions to Mars will include wind sensors similars in concept to the REMS instrument wind sensor. In the TWINS (Temperature and Wind sensors for InSight mission) instrument of InSight NASA mission (expected for 2018) the temperature and wind sensors from the REMS instrument will be refurbished, with enhanced performance in terms of dynamic range

and resolution [3]. In turn, NASA's Mars2020 mission will include the MEDA (Mars Environmental Dynamical Analyzer) device, whose working principle will be again thermal anemoemtry. Therefore, the thermal characterization of the wind sensors proposed is of great interest.

On the other hand, it is known that microelectromechanical systems (MEMS) devices suffer from the undesired effect of charge trapped in their dielectric layer. This slow charging process has been associated to the diffusion phenomena [4, 5]. The analysis of the charging dynamics is an important issue that has been widely studied [6, 7, 8]. In this Thesis, the characterization of the net charge trapped in the dielectric layer of an electrostatic contactless MEMS for different voltage actuations is presented.

Both types of systems have been modeled using Diffusive Representation (DR). Diffusive representation is a mathematical tool that allows the description of any physical phenomena based on diffusion using state-space models of arbitrary order in the frequency domain. In the literature, it has been used in multiple appications, such as power electronics [9], acoustics [10] or biology [11]. The methodology is suitable for fractional nature systems. (A fractional-order system is a dynamical system that can be modeled by a fractional differential equation containing derivatives of non-integer order). The behavioural models obtained with diffusive representation are useful in the analysis and prediction of the closed-loop control response, using the sliding mode analysis, which has been also studied during the work of this Thesis. The diffusive representation method is fully explained in section 2.2.5.

For these systems modeling, a type of signal with beneficial properties in system identification has been used: Pseudo Random Binary Sequences (PRBS). These type of signals are used throughout all the experimental measurements carried out for the study of the aforementioned systems. A detailed description of this type of signal is presented in section 2.2.4.

As mentioned before, the theory of Sliding Mode Controllers (SMC) has also been applied for the prediction of the closed-loop dynamics of the wind sensors that have been thermally characterized. The sliding mode control technique is a state space-based discontinuous feedback control method. In this regard, no specific design of a sliding mode controller has been made, but the analysis of the resulting dynamics is made using the tools of equivalent control typical of sliding mode controllers. This analysis is of great interest since helps to understand better the dynamics of these sensors and theoretically explains how the time response of these type of sensors can be improved.

1.2   Objectives

The main objective of this Thesis is to contribute to the modeling of diffusive behaviour systems. The objectives for the research work can be listed as following:

- *Analysis and modeling of a thermal anemometer.* Characterization of the thermal dynamics of different prototypes of a 3-dimensional spherical wind sensor as a function of the wind velocity applied, by using an state-space representation approach.

- *Characterization of time-varying system dynamics.* Develop the Diffusive Representation

theory for the time-varying case that enables the obtention of the models of the sytem for time-changing situations from single experiments.

- *Sliding mode analysis of the closed-loop dynamics of a thermal anemometer.* From the sliding mode controllers theory and using an state-space variables representation, understand and predict the closed-loop dynamics under constant temperature operation mode of a 3-dimensional wind sensor.

- *Sliding mode analysis for improving the time response of a thermal sensor.* Theoretically explain, with the sliding mode analysis and the study of the matched and unmatched disturbances of a system, how the time response of a 3-dimensional spherical wind sensor can be enhanced.

- *Analysis and modeling of the prototype of the REMS wind sensor.* Characterization of the time-varying thermal dynamics of the engineering model prototype of the REMS wind sensor as a function of the wind velocity applied.

- *Study of the cross-coupling effects in a thermal anemometer.* Characterize and understand the self-heating and cross-heating effects between different components of a thermal wind sensor.

- *Dielectric charge analysis and modeling.* Characterization of the charge dynamics by a state-space representation approach. Obtention of the charge evolution under different bias voltages.

1.3 Methodology

The methodology employed is different whether the thermal analysis of the wind sensors or the characterization of the dielectric charge of the MEMS devices is being performed.

In the thermal analysis of the 3-dimensional spherical wind sensors developed by the UPC team, the necessary measurements for the characterization have been carried out at the UPC wind tunnel facilities. This wind tunnel consists in an stainless steel hypobaric chamber with an automatic fan located in front of the sensor that provides the necessary wind velocities for the study. The pressure in the chamber is adjusted so that the combination of the air ambient temperature, pressure and velocities inside are the most similar to the conditions presented in Mars atmosphere, although the use of CO_2 gas was discarded for simplicity of the system.

The operational design of one of these prototypes was also tested in Aarhus University (Danmark) facilities, where the wind sensor was succesfully tested in Martian like conditions. Wind velocities from 1m/s up to 13m/s, 10mBar CO_2 pressure and temperatures until -18°C were employed in the measurements. The wind velocities in this cases were also obtained from a wind fan that generated the necessary laminar flow of the air.

For the thermal analysis of the engineering model of the REMS wind sensor, the experimental measurements were performed at the wind tunnel facilities of Centro de Astrobilogía (CAB, CSIC-INTA), located in INTA dependencies in Torrejón de Ardoz (Madrid). The operation mode of this

wind tunnel is different from the ones in UPC and Aarhus. Due to its linear geometry, the exact wind velocities are obtained from the sensor movement along the tunnel instead of moving the air with a wind fan. Nevertheless, the time-varying modeling demonstranted to be also valid in this case.

Extensive experimental measurements have been made to extract dynamical models. In the UPC and CAB facilities experimental setups, the wind sensors were controlled with a National Instruments' FPGA installed outside the wind tunnel. The FPGA, programmed in Labview environment, provided both open and closed-loop operation modes for the analysis. The necessary currents were provided by two National Instruments current sources. In Aarhus University facilities, however, an specific measurement circuit had to be designed and implemented. In this occasion, a microcontroller programmed in C language was used for the control of the sensor. In order to process all these measurements and extract the models, MATLAB programming has been used.

In the charcterization of the trapped charge in the dielectric layer of a MEMS device, the experimental setup consisted in a Keysight E4980a precision LCR meter which made capacitance measurements and also applied smart device actuations. The device was connected to a computer, which implemented the necessary control. The equipment used to carry out the experiments included other laboratory stuff, such as a probe station, an impedance anayzer Agilent 4294A and an ambient control chamber, among others. As in the thermal analysis case, the measurements were processed with MATLAB.

1.4   Document Organization

The research work done along this Thesis is presented as a compendium of publications. After this chapter, which contains an introduction to the work carried out during the Thesis, the remaining of this document is organized as follows.

- Chapter 2 describes the background of this Thesis. In this chapter it can be found the most significant contributions regarding to the four main topics of this work: wind sensing in Mars, thermal system identification methods, sliding mode controllers and dielectric charging in contactless MEMS.

- Chapter 3 contains the full text of the publications conforming the compendium. It is composed of four publications in JCR-indexed scientific journals.

- Chapter 4 includes other Thesis-related work. Specifically a report that contains the characterization of the thermal dynamics of the engineering model prototype of the REMS wind sensor under different wind velocities is presented. It also contains the characterization of the cross-coupling effects between different parts of the structure of the aforementioned sensor. These are the main results obtained during a short stay in the Centro de Astrobiología (CAB, CSIC-INTA) in Madrid.

- Chapter 5 draws the main conclusions derived from the results of the Thesis work. It also

includes a future work section, which highlights potential research lines outlined from this work.

- Appendix A includes some workshop and conference publications related to the research work of this Thesis, and not included in the compendium.

Bibliography

[1] J. Gómez-Elvira, C. Armiens, L. Castañer, M. Domínguez, M. Genzer, F. Gómez, R. Haberle, A.-M. Harri, V. Jiménez, H. Kahanpää, L. Kowalski, A. Lepinette, J. Martín, J. Martínez-Frías, I. McEwan, L. Mora, J. Moreno, S. Navarro, M. A. de Pablo, V. Peinado, A. Peña, J. Polkko, M. Ramos, N. O. Renno, J. Ricart, M. Richardson, J. Rodríguez-Manfredi, J. Romeral, E. Sebastián, J. Serrano, M. de la Torre Juárez, J. Torres, F. Torrero, R. Urquí, L. Vázquez, T. Velasco, J. Verdasca, M.-P. Zorzano, and J. Martín-Torres. Rems: The environmental sensor suite for the mars science laboratory rover. *Space Science Reviews*, 170(1):583–640, 2012. ISSN 1572-9672.

[2] Y. Zhu, B. Chen, M. Qin, and Q. A. Huang. 2-d micromachined thermal wind sensors: A review. *IEEE Internet of Things Journal*, 1(3):216–232, June 2014. ISSN 2327-4662.

[3] T. Velasco and J. A. Rodríguez-Manfredi. The TWINS Instrument On Board Mars Insight Mission. In *EGU General Assembly Conference Abstracts*, volume 17 of *EGU General Assembly Conference Abstracts*, page 2571, April 2015.

[4] R. W. Herfst, P. G. Steeneken, J. Schmitz, A. J. G. Mank, and M. van Gils. Kelvin probe study of laterally inhomogeneous dielectric charging and charge diffusion in rf mems capacitive switches. In *2008 IEEE International Reliability Physics Symposium*, pages 492–495, April 2008.

[5] R.W. Herfst, P.G. Steeneken, and J. Schmitz. Time and voltage dependence of dielectric charging in RF MEMS capacitive switches. In *IEEE 45th Annual Int. Reliability Physics Symp., Phoenix*, pages 417–421, 2007.

[6] R. W. Herfst, P. G. Steeneken, H. G. A. Huizing, and J. Schmitz. Center-shift method for the characterization of dielectric charging in rf mems capacitive switches. *IEEE Transactions on Semiconductor Manufacturing*, 21(2):148–153, May 2008. ISSN 0894-6507.

[7] X. Yuan, J.C.M. Hwang, D. Forehand, and C.L. Goldsmith. Modeling and characterization of dielectric-charging effects in RF MEMS capacitive switches. In *Digest of IEEE MTT-S 2005 Microwave Symposium Digest*, pages 753–756, 2005.

[8] U. Zaghloul, G. Papaioannou, F. Coccetti, P. Pons, and R. Plana. Dielectric charging in silicon nitride films for mems capacitive switches: Effect of film thickness and deposition conditions. *Microelectronics Reliability*, 49(9):1309 – 1314, 2009. ISSN 0026-2714. 20th European Symposium on the Reliability of Electron Devices, Failure Physics and Analysis.

[9] B. Allard, X. Jorda, P. Bidan, A. Rumeau, H. Morel, X. Perpina, M. Vellvehi, and S. M'Rad. Reduced-order thermal behavioral model based on diffusive representation. *IEEE Transactions on Power Electronics*, 24(12):2833–2846, Dec 2009. ISSN 0885-8993.

[10] Th. Helié and D. Matignon. Diffusive representations for the analysis and simulation of flared acoustic pipes with visco-thermal losses. *Mathematical Models and Methods in Applied Sciences*, 16(04):503–536, 2006.

[11] C. Casenave and G. Montseny. Identification of nonlinear volterra models by means of diffusive representation. *IFAC Proceedings Volumes*, 41(2):4024 – 4029, 2008. ISSN 1474-6670. 17th IFAC World Congress.

Chapter 2

Thesis Background

This chapter aims to be the background of the work carried out during this Thesis. The chapter focuses in explaining the state of the art and the methodologies employed along the main topics related to the research work.

The chapter will be divided in four main sections: wind sensing in Mars, thermal system identification, sliding mode controllers and dielectric charging in contactless MEMS. These four topics have been of relevance in the development of this Thesis.

2.1 Wind Sensing in Mars

The exploration of the Mars planet has been for interest for the scientific community for years. More than 40 space missions have aimed to explore the Red planet, but only half of them have been a success. The objective of these missions consist mostly in gathering information about atmospherical and geological processes and search for biological material, among others, in Mars. Wind velocity information is in the scope of such missions. It is known that Mars atmosphere is very different from the atmosphere of the Earth. Much more lighter, and mostly composed of CO_2, its pressure is 150 times lower than in Earth. In general, the pressure in Mars is in the range of 6-12 mBar and there is a large temperature dynamical range from 150 to 300K [1, 2]. These characteristics produce significant heat flux and radiation processes, where the wind detection is fundamental for the understanding of those meteorological processes.

Wind velocity detection in Mars started in the seventies. Most of the information available nowadays about wind velocity in Mars comes from the successful missions that involved landers or rovers on Mars surface. Some of the missions equipped with wind detection instruments are the followings: Viking 1 and 2 (both landed in Mars in 1976), Mars Pathfinder (1997), Phoenix (2008) and Mars Science Laboratory (MSL) (2012). In 2016, ExoMars mission of European Space Agency (ESA) that was launched to Mars included a suite of sensors, among which was the MetWind, a sensor oriented to measure wind speed and direction. However, as the landing failed, no wind data was received.

Thermal anemometry is the method that has been mostly used for wind sensing in Mars. It was the method chosen for Viking, Pathfinder, Curiosity and also in the failed ExoMars missions. On the contrary, Phoenix lander used a wind sock [3], where the images capted from a camera where used for the inference of wind velocity and angle.

2.1.1 Thermal Anemometry

Thermal anemometry detects the wind velocity by measuring the power losses of a heated element due to forced convection [4]. This method stands out for its robustness and simplicity. Thermal anemometers can work in open or closed loop operation mode. Changes in wind velocity generate changes in the convection heat transfer of the heated structure. For instance, if a constant power is dissipated in the sensor, increasing wind speed will decrease the temperature in the sensor. This is the open-loop mode of operation CPA (Constant Power Anemometry). In order to improve the time response of the system, though, these sensors are usually operated at constant temperature. In the closed-loop mode, a heating element is maintained at a constant temperature (over ambient temperature) and the changes in wind speed are compensated by the temperature control loop. An increase (decrease) in wind speed requires more (less) power dissipation in the sensors. The injected power is then the output signal of the system. The wind velocity is calculated from the thermal conductance (ratio of the power and the temperature difference between the hot point and the ambient) which is related to the Nusselt number (embodying the Reynolds number and hence the wind speed). It is known that open-loop mode is slow in terms of time response, and therefore, constant temperature anemometry (CTA) mode is the most extended method for sensing wind velocity [5].

2.1.2 Viking Wind Sensor Unit

Both Viking landers (I and II) were equipped with thermal hot-film anemometers. The MSA (Meteorological Sensor Assembly) consisted in a quadrant sensor, that gave wind direction information, a hot-film sensor array for wind velocity detection, and a reference temperature sensor for measuring the ambient temperature. The wind speed sensors were two small cylinders covered by a thin film of platinum (Pt) that formed a resistance. Each cylinder had a length of 10.2 mm and a diameter of 0.51 mm and was covered with a 0.635 μm thickness Pt film. These sensors were mounted at 90° with respect to each other and worked under constant temperature operation with an overheat of 100°C above the ambient temperature (given by the reference sensor). The wind velocity, normal to the sensor, was determined by measuring the power dissipated within the sensor element (CTA mode) [6]. The quadrant sensor provided wind direction in an independent measurement. It was formed by a heated post and four thermocouple junctions mounted around the assembly. The central post, also controlled with an overheat of 100°C above the temperature reference sensor, and the opposing thermocouple junctions were connected in series so that each pair measured the temperature difference across the sensor due to the thermal wake in the post [6].

The MSA was supported by the Meteorological Boom Assembly (MBA), which consisted in
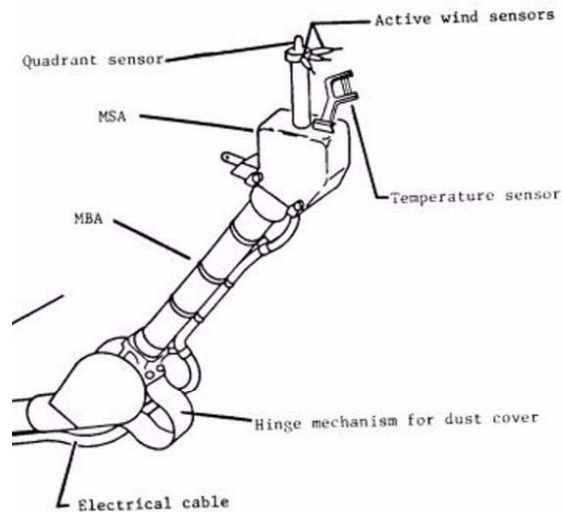
Figure 2.1: Viking Meteorological Boom Assembly schema [6].

a deployable structure, called boom, which was in a stowed position during the launch, cruise and entry portions of the mission. After landing, the boom is released and adquires an extended position. In Figure 2.1, an schema of the Viking MBA can be observed.

In the overall Viking mission, an extense view of Mars was achieved. Volcanos, canyons, craters, wind-formed features and evidence of surface water images were received. Besides, the temperature at the landing site (from 155 to 250K), dust storms, surface winds and seasonal pressure changes were also observed [7, 8].

2.1.3 Mars Pathfinder Wind Sensor Unit

The Mars Pathfinder included the Atmospheric Structure Instrument (ASI) and the Meteorology Package (MET) instruments. While the ASI was designed to study the atmospheric structure of Mars while descending, the MET was designed to study the meteorological conditions at the surface after landing. During the entry in Mars atmosphere, the data collected allowed the reconstruction of the profiles of atmospheric density, temperature and pressure. On the ground, the Meteorology Package collected temperature, pressure, and wind data for use in the study and characterization of diurnal and longer term variations of the atmosphere [9]. For this task, a meteorology mast was deployed on the landing site. This mast of 1.1 m height, included temperature sensors and a wind sensor based on hot-wire anemometry on its top. The wind velocity was also intended to be measured from a set of wind-socks mounted on the mast at intermediate heights.

On the one hand, the wind sensor on the top of the mast consisted of six identical hot wire elements of 0.9 platinum − 0.1 iridium alloy of 65 μm of diameter, distributed uniformly around a circular cylinder [10]. The six elements, connected in series, were operated in CCA (Constant Current Anemometry) mode (in open-loop), where a continuous current of 51.5 mA was injected and

heated the elements 40°C above ambient temperature in still CO_2 Martian surface pressures. The wind velocity was detected from the overall cooling of the wires when they were exposed to wind, while the wind direction detection was based on the temperature differences between the segments. Wire temperature changes were accompanied by wire resistance changes and were measured by the voltage drops across each segment.

To complement the measurements, three wind socks were located at various heights of the mast to determine the speed and direction of the winds at the landing site. An imaging system took pictures of the wind socks repeatedly. From the images, the wind velocity, at three heights above the surface, was measured from the orientations of the wind socks in the images. This information was used to estimate the aerodynamic roughness of the surface in the vicinity of the lander, and to determine the variation in wind speed with height. The vertical wind profile was intended to help to develop and modify theories of how dust and sand particles are lifted into the martian atmosphere by winds, for example [9].

The Pathfinder ASI/MET instruments were designed for measuring wind speed to within 1 m/s at low wind speeds and within 4 m/s above 20 m/s, with an accuracy of 0.25°C in the overheat measurement. The sensor was designed for wind directional variations as small as 10°. However, such an accurate wind speed determination required a further calibration of the relation between wind velocity, air temperature and the hot-wire overheat of the sensor under Mars surface conditions. As all these requirements were not available, only direction data was obtained [11].

2.1.4   MSL Wind Sensor Unit

In August 2012, succesfully landed on Mars surface the Curiosity rover from the Mars Science Laboratory (MSL) mission. Among all the science devices, it included the REMS (Remote Environmental Monitoring Station) instrument, a weather monitoring system. Still operating, it provides atmosphere pressure, humidity, ultraviolet radiation, air and ground temperatures and wind velocity and direction measurements [12, 13].

For the wind velocity and direction detection, platinum resistors, fabricated on silicon technology, were employed. These resistors were grouped in sets of four in a square configuration to achieve 2-dimensional wind sensitivity. These dice-sets are called 2-D Wind Transducers (WT). To obtain the 3-dimensional direction, three of these sets were placed at 120° with each other in a cylindrical boom. The three wind transducers form a Wind Sensor (WS) unit. A suitable combination of all wind transducers output signals provide the absolute wind speed value and direction.

The four dice of each Wind Tranduscer are based on hot film anemometry, working in CTA mode. These dice are kept at a fixed temperature difference with respect to a reference die (cold die) using an electro-thermal sigma-delta control loop which supplies power to the hot die. The circuit measures the power delivered to the hot die, and from the temperature difference with the reference die, the thermal conductance from the hot die to the CO_2 ambient is computed. In order to do this, additional thermal information to calculate the power lost by conduction through the supports and the wire-bonding is required, as well as thermal ambient information to evaluate radiation losses [5, 14]. Two booms, with a Wind Sensor unit each, were incoporated in the rover
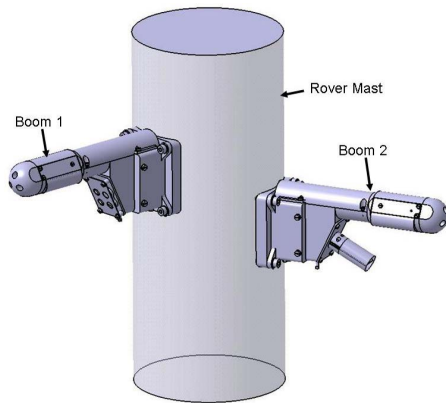
Figure 2.2: REMS wind sensor mast and booms [14].
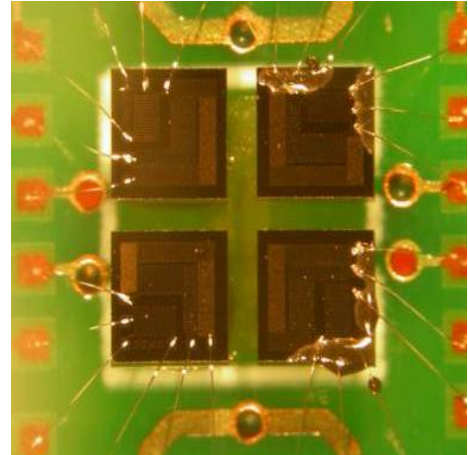
Figure 2.3: REMS wind sensor Wind Transducer

mast to characterize air flow near the Martian surface from breezes, dust devils, and dust storms [15]. The booms were designed to support the Wind Sensor units in order to reduce aerodynamic effects and minimize weight. They were placed at an angle of 120°, and located at 50 height of difference. The different locations of the booms were intended to ensure that the perturbation from the mast only affected one sensor unit at a time, as the wind is measured from all directions [14]. In Figures 2.2 and 2.3 an schema of the booms and one dice-set can be observed respectively.

Among the characteristics of the REMS wind sensor, it can measure horizontal wind speed in the range [0 - 70]m/s while vertical wind speed is within the range [0 - 10]m/s, both velocities with an accuracy of 0.5m/s. The wind direction is in the range [0° - 360°], in the 3-dimensional full recovery, with a resolution of 30°.

It has to be mentioned that in the landing process one of the Wind Sensor (WS) units was damaged, probably by a stone impact. However, thanks to the remaining Wind Sensor unit, it has been possible to receive and characterize wind data from Mars.

In this Thesis, a prototype of the engineering model, developed in 2008, that lead to the flight model of the REMS wind sensor has been thermally characterized. The results from the analysis can be encountered at chapter 4.

2.1.5 ExoMars Wind Sensor Unit

The main objectives of the ExoMars mission were two. One was to search for evidence of methane and also to trace atmospheric gases that could show any biological or geological processes. The other was to test the technologies for subsequent ESA missions to Mars.

As payload, DREAMS (Dust Characterization, Risk Assessment, and Environment Analyser on the Martian Surface) package was included. It consisted of a suite of sensors to measure humidity, pressure, surface temperature, transparency of the atmosphere, atmospheric electrification and

wind speed and direction (MetWind) [16].

The Metwind sensor consisted of a sensor head and an electronics board. The measurement process was based on a thermal anemometry approach, similar to that used on Mars Pathfinder, and was a re-flight of the Wind Sensor of the unlucky mission Beagle 2 from ESA [17].

The sensor head included three thin-film platinum heat transfer gauges, uniformly spaced on a vertical cylinder. The thermal anemometry mode designed was CCA, raising the heated elements' temperature above the ambient. The temperature of each hot film was calculated by measuring the electrical resistance of the thin-films. The differences in heat transfer coefficients between the three films was used to calculate a 2-dimensional wind vector perpendicular to the axis of the wind sensor [16]. However, as the landing process failed, no wind information was received from this mission.

2.1.6   UPC 3-D Hot Sphere Anemometer

Although the wind sensors presented in this section do not belong to any flight mission to Mars, they are an important part of this Thesis and therefore, will be described.

Since 2008, the Micro and Nano Technologies (MNT) group from Universitat Politècncica de Catalunya (UPC) has gone on the trail of a new wind sensor for the Mars atmosphere. The goal since then has been to present an engineering concept of a 3-dimensional (3-D) spherical wind sensor to satisfy robustness and power efficiency constraints. In recent years, several prototypes have been fabricated to achieve these objectives. In chapter 3, section 3.3, the analysis of the improvement in the dynamical response between two of these prototypes is presented.

Classically, 3-dimensional wind detection is achieved measuring the tangential component of the wind from several 2-dimensional anemometers, as explained in subsections 2.1.3, 2.1.4 and 2.1.5. The main disadvantage of this method is that to compute 3-dimensional wind, complex retrieval algorithms are needed. Not to mention that they also need more sensing elements, increasing cost and complexity. However, a spherical wind sensor benefits from the inherent isotropy, axis-symmetry and an ideal wind flow geometry in the heat dissipation [18, 19].

In this subsection we will briefly explain the particularities of the two sensors described in 3.3 and of interest for this Thesis. An schema and a photography of the two sensors are shown in Figures 2.4 and 2.5 respectively.

A initially designed sensor is composed of two silver hemispheres connected to two 'back to back' PCBs (Printed Circuit Board), which provide mechanical and electrical support. In order to reduce emissivity and avoid oxidation, the hemispheres are polished and sputtered with a thin layer of gold ($\approx$ 100 nm) on their surface. Each of the hemispheres has a mass of 1.2 g and a thickness of 0.6 mm. The diameter of the sphere formed by the two hemispheres is of 10 mm. Each hemisphere, integrates a SMD (Surface Mounted Device) Pt resistor. The resistors, R_A and R_B, allow to heat the hemispheres and sense the temperature. In the PCBs, two more Pt resistors are attached, R_{core_1} and R_{core_2}, in order to heat the core of the sphere to reduce the conduction heat flux between the hemispheres and the supporting structure. The resistors of this sensor are commercial surface mounted 100 Ω platinum resistors with temperature coefficient $\alpha = 0.00385°C^{-1}$ with different
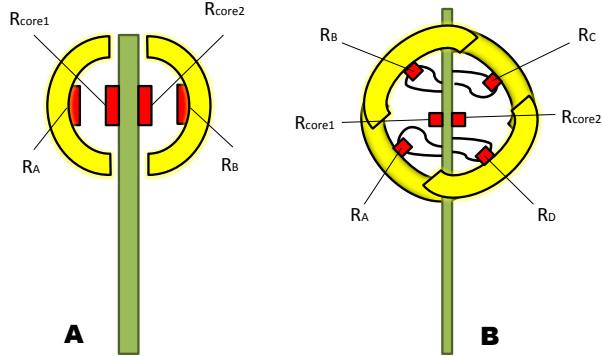
Figure 2.4: Schema of two protoypes of the spherical anemometer
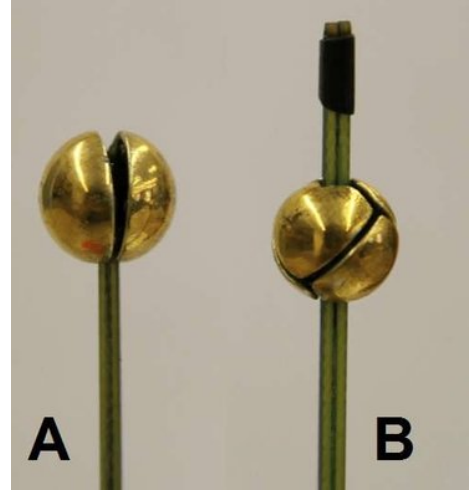
Figure 2.5: Photo of two protoypes of the spherical anemometer

encapsulations; SMD0603 for the spherical sectors and SMD0805 for the PCB. This sensor is named *A* in both Figures 2.4 and 2.5.

The last protoype designed so far, is composed of four silver sectors connected to two 'back to back' PCBs. Now, the silver sectors (which have the same polishing and sputtering process as the two hemispheres prototype), form a tetrahedral sphere of 10 mm. A detailed description of the sensor structure, sectors support and sensor construction is found in chapter 3 in section 3.2. Each sector in this case has a mass of 0.5 g and thickness 0.6 mm. Again, each sector and the PCBs have a Pt resistor integrated on them (R_A, R_B, R_C and R_D in the sectors, and R_{core_1} and R_{core_2} in the PCBs) which allow heating and sensing of the temperature and reducing conduction heat flux. A key design factor for improving the time response of the sensor is to ensure a good thermal connection between heaters and sectors. To achieve this goal, non-encapsulated chip resistors with no thermal insulators were used this time. Additionaly, the electrical connections between the PCBs and the resistors are made by a wire bonding process. For this purpose, resistor chips were fabricated at Universitat Politècnica de Catalunya clean room facilities from silicon wafers. Silicon oxide (SiO_2) was grown thermally for electrical isolation. On top of the SiO_2, the platinum resistors were patterned with a photolitography process. The Pt resistors of the four sectors prototype have a nominal value of 175 Ω at 0°C and a temperature coefficient $\alpha = 0.0031°C^{-1}$. This sensor is named *B* in both Figures 2.4 and 2.5.

2.1.7 Future Missions Wind Sensor Units

Future missions to Mars, currently in development, will include wind sensing equipment. One of these missions is the InSight (Interior Exploration using Seismic Investigations, Geodesy and Heat Transport) that will place a single geophysical lander on Mars to study its deep interior. It will

include environmental characterization sensors, such as a temperature sensor and a wind sensor, that will conform the TWINS (Temperaure and Wind Sensors for Insight) instrument. It will be directly refurbished from REMS spare hardware, with some enhanced features, such as an optimized temperature range, a more efficient power consumption and improved calibration [20].

On the other hand, Mars 2020 Rover mission from NASA, will place a lander on Mars surface with the objective of seeking ancient past habitable conditions and signs of past microbial life. It will include the MEDA (Mars Environmental Dynamics Analyzer) instrument with the aim of measuring weather and monitoring the dusty environment of Mars surface. The MEDA will be conformed by a radiation/dust sensor, a pressure sensor, an air temperature sensor, a thermal infrared sensor for measuring downward and upward thermal infrared radiation as well as surface skin temperature, a relative humidity sensor and two wind sensors [21].

The wind sensors will be positioned in two booms oriented at 120 degrees from each other. The booms will be located around a mast, where some of the other mentioned sensors will be placed. The MEDA wind sensor is an heritage from the REMS wind sensor, and therefore, the same device concept, although including many significant changes in structure and number of sensors, is being carried out.

The MEDA wind sensor takes relevance in this Thesis due to the fact that the design, fabrication and characterization of the silicon chips that will be used as the heating elements in the flight model wind sensor of the mission, have been developed in paralell to the work of this Thesis.

2.2 Thermal System Identification

When describing the behaviour of a system, a physical model based on the fundamental physical laws can be built, but in many cases, due to the complex nature of many systems, these models will be impossible to solve in reasonable time. A common approach, therefore, is to try to determine a mathematical relation between the input and output measurements without going into the details of what is actually happening inside the system.

Finding a mathematical model from observed data is fundamental in science and engineering. From a system's input and output measurements, system identification methodology builds a mathematical model of a dynamic system. In a dynamic system, the values of the output signals depend on both the instantaneous values of its input signals and also on the past behaviour of the system. Models of dynamic systems are typically described by differential or difference equations, transfer functions, state-space equations or pole-zero-gain models. These models can be represented both in continuous-time and discrete-time form.

In this Thesis, we will thermally characterize a wind sensor based on thermal anemometry, therefore, we will focus on the existing methods for thermal systems modeling. The thermal effects on electronic systems have been widely studied. They have been studied from the semiconductors level [22] up to the whole system [23, 24]. Analyzing a global thermal problem in detail is of great complexity due to the fact that effects such as conduction, convection and radiation heat transfers must be taken into account. The Partial Differential Equation (PDE) heat equation allows to study

the heat distribution of a thermal system in a given region over time:

$$\frac{\partial u}{\partial t} - \alpha\left(\frac{\partial^2 u}{\partial x^2} + \frac{\partial^2 u}{\partial y^2} + \frac{\partial^2 u}{\partial z^2}\right) = \frac{Q(x, y, z, t)}{c_p \rho} \tag{2.1}$$

where $u = u(x, y, z, t)$ represents the temperature in an isotropic and homogeneous medium in a 3-dimensional space. The thermal diffusivity is $\alpha = \frac{k}{\rho c_p}$, with k the thermal conductivity, ρ is the mass density and c_p is the specific heat capacity of the material. $Q(x, y, z, t)$ is the heat energy per unit volume and per unit time, that represents the external sources or sinks of heat energy. The analytical solution of this problem generally requires the solution to boundary value problems, which complicates its solution.

Heat conduction has a long memory behaviour, which means that the current state of the system depends on the previous ones. Modeling of these type of systems is widely encountered in the literature. In the following subsections some of the modeling methods of thermal systems are briefly explained. Among the presented methods, we will focus on Diffusive Representation theory, the method used in the characterization of the wind sensors of this Thesis.

2.2.1 Finite Element Analysis

The solution to the heat equation can be obtained applying the finite element method (FEM). FEM is an appropiate method for solving a wide range of multiphysical processes, such as electrical, magnetical and thermal processes. The analysis of a 3-dimensional system can be performed by dividing the system into a finite set of elements and assigning to each element a compact model. This process is known as meshing. The meshing method approximates the PDEs with numerical model equations, which can be solved using numerical methods. These solutions are, in fact, an approximation of the real solution to the PDEs.

For example, we can consider $u(x, t)$ as the 1-dimensional temperature along the lenght x of a rod that is non-uniformly heated. The function u can be approximated by a function u_h using linear combinations of basis functions according to:

$$\begin{aligned} u &\approx u_h \\ u_h &= \sum_i u_i \chi_i \end{aligned} \tag{2.2}$$

where χ_i denotes the basis functions and u_i denotes the coefficients of the functions that approximate u with u_h.

Finite element modeling works well on diffusive systems in general. In the case that concern us, FEM has been commonly used in thermal analysis. In [25] the thermal behaviour of a DC/DC converter is modeled using this technique. In [26], it was also used for the analysis of the temperature distribution of a lithium-ion battery in thermal abuse applications. The charge and discharge thermal behaviour of a battery was also discussed in [27]. In [28], the finite element analysis was used

for automatically extract a compact thermal model of a test power module. Thermal wind sensor's behaviour has also been analyzed with 3-dimensional FEM models, as in the case of [29], where the thermal-mechanical reliability of the package of a MEMS thermal wind sensor was presented.

However, simulating a finite element model requires knowing all the thermal characteristics (specific heat, thermal conductivity, density) and to set boundary conditions of the studied thermal system. Hence, it requires many prior experiments for thermal characterization. In spite of this, non-ideal boundaries, nonlinear dynamical behaviours and exact geometries from the thermal system have to be taken into account in the analysis. Besides, processing is usually computer intensive due to the large modeling size.

2.2.2 Thermal Equivalent Circuit Models

For the analysis of a thermal system, an electrical analogue where temperature is alike to voltage and power is alike to current, can be used. In a thermal system, when power is injected into the heat sources, the resulting temperature variation is measured. The complex thermal impedance, Z_{th}, is the transfer function that relates the power and temperature in the frequency domain as follows:

$$Z_{th}(\omega) = \frac{T(\omega)}{Q(\omega)} \tag{2.3}$$

where $T(\omega)$ is the output temperature, $Q(\omega)$ is the input power and ω is the angular frequency.

Physically derived lumped parameter models

The lumped element model or lumped parameter model, simplifies the behaviour of a spatially distributed system into a topology of discrete entities. The PDEs of the physical system are reduced to ordinary differential equations (ODE)s with a finite number of parameters. These types of thermal equivalent circuits are designed to match the physical structure of a system. The system is considered a set of thermal homogeneous regions (or lumps) which are modeled as capacitors (akin to heat capacity). The lumps are interconnected with their neighbours using resistors (akin to thermal resistances). The heat dissipation is modeled as a current source that results in heat flux (analogue to electric current) flowing through the equivalent circuit and giving rise to a temperature difference (analogue to voltage) across components [30]. The result of this modeling is referred as a lumped parameter model. In [31], a thermal circuit anologue was presented, where an inductor for power electronic systems was modeled. In [32], the temperature estimation of interior permanent magnet synchronous motors was done using these thermal circuit equivalents. In the semiconductors field, in [22], the self-heating effect in MOSFETs was modeled with the lumped modeling methodology.

Equivalent circuit thermal analogues

The most typical topologies used in thermal modeling are the Cauer and Foster based networks. These networks, are mathematically identical in their one-port form [33]. Whilst the Cauer network
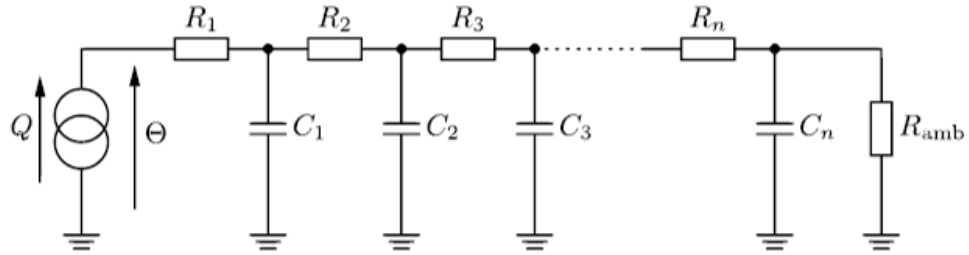
Figure 2.6: Cauer thermal equivalent circuit [30].

is closer to the physical form of the thermal circuit form because each node represents a real temperature, in the Foster network, only the the overall temperature behaviours between the measured points can be guaranteed [34]. Besides, Cauer networks are much more general due to the fact that Foster networks can only model self-impedance as they are an only one-port networks [30]. In Figures 2.6 and 2.7 the classical Cauer and Foster networks are shown.

The Cauer network reflects the real physical setup of the thermal device based on thermal capacitances with intermediary thermal resistances. In order to build a model of a complete thermal system, the system is first divided into single material blocks, each of which is assigned a thermal resistance and capacitance. The complete system model is formed by interconnecting these blocks and inserting heat sources and ambient connections as appropriate. Typically, each single material is modeled as a single RC element, which can also be done in 3-dimensional geometries. These nodes allow access to internal temperatures of layers of the material, and therefore, they have a physical significance and represent the temperature at a physical location. Foster network, in contrast, is independent of the internal structure of the material and the individual RC elements of the circuit do not represent any physical property, as they only represent a time constant present in the network [30].
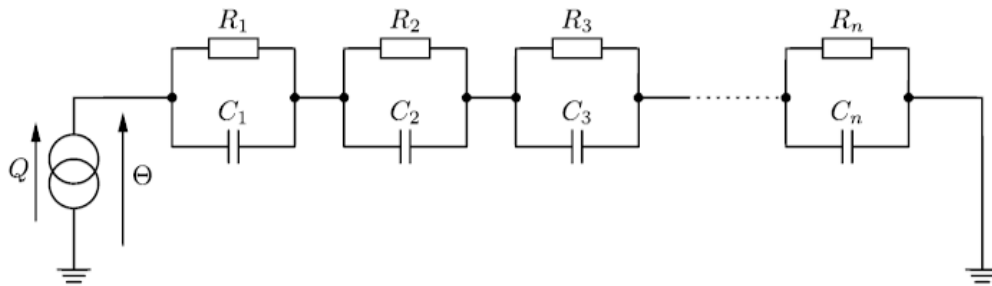
Figure 2.7: Foster thermal equivalent circuit [30].
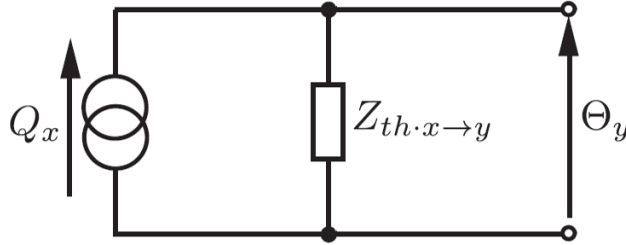
Figure 2.8: Norton equivalent circuit of the thermal circuit between heat source x and measurement point y [36].

Although a variety of thermal networks can be used, they can all be simplified into a Norton equivalent circuit with frequency dependant impedance. (See Figure 2.8) [35].

It can be observed that the increase of temperature at y occurs due to heat source x and it is $\Theta_y = Z_{th_{x \longmapsto y}} Q_x$. The temperature at y due to all heat sources is calculated by superposition:

$$\Theta_y = \sum_x Z_{th_{x \longmapsto y}} Q_x \tag{2.4}$$

where the thermal transfer impedance $Z_{th_{x \longmapsto y}}$ is the cross-coupling between x and y. Once it is identified, cross-coupling characteristics can be used to predict and model the temperature at each system element due to the power dissipations in all the elements.

Equivalent circuit thermal analogues have been widely used. In [37] a HEV/EV battery thermal model using a Foster network is proposed. In [38] an electrical analogue of a voltage source converter module is used to estimate the junction temperatures of semiconductor devices. In [39], the Cauer network is proposed to obtain the nonlinear compact thermal model of power semiconductor devices. Similarly in [40], thermal impedance spectroscopy is used to assess the required number of the Cauer network elements to model a single material block. In [36] the thermal cross-coupling responses between the multiple elements of a thermal system are obtained based on a Norton equivalent circuit.

2.2.3   First Principles Model Derivation

From the mathematical first principles, the thermal analysis of a system can also be performed. This approach usually relies on solving the heat equation given in equation (2.1). For example, in [41], the heat equation was applied to obtain the physical model of a power electronic module with the intention of predicting the temperature response due to cross-coupling between devices. In [41] and [42] the thermal models based on the Fourier series are an analytical solution to the 3-dimensional heat equation, where the solution uses the Fourier cosine series expansion to reduce the mathematical complexity. In [43], a 2-dimensional physical model for power bipolar devices, such as IEGT (injection-enhanced gate transistor) devices, is obtained by solving the diffusion
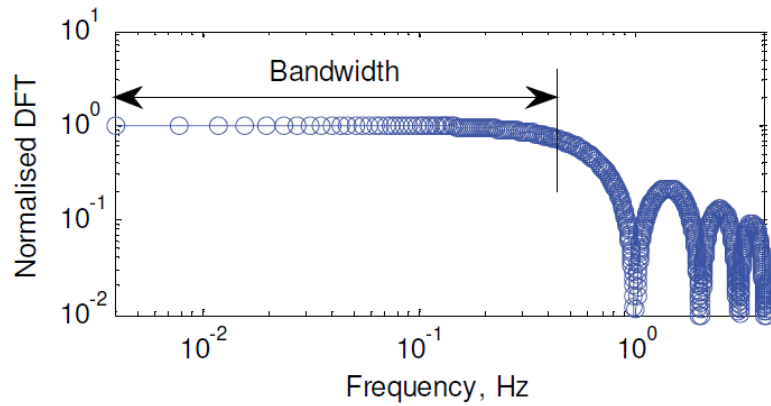
Figure 2.9: Normalised Discrete Fourier Transform (DFT) of a PRBS sequence showing the flat region up to the band limit[50]

equation. Although it is an effective method to model thermal effects, it can be quite complex mathematically.

2.2.4 Pseudo Random Binary Sequences in System Identification

This subsection is intended to explain a type of input signals very useful in thermal identification analysis.

Pseudo Random Binary Sequence (PRBS) techniques are an appropriate alternative to step response testing because they have proven to be noise resilience in thermal identification problems [44, 45] thanks to the wide frequency spectrum of these type of signals. They have been used in system identification for many decades. In [46] an in-depth analysis of the technique and its application is presented. This technique has been applied to a variety of applications, including parameter estimation in electrical generators [47], testing digital-to-analogue converters [48], and modeling of batteries [49].

PRBSs are finite-lenght predetermined signals of pseudo aleatory '0's and '1's (or two predefined
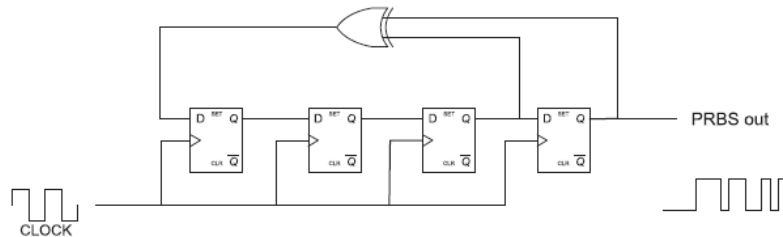
Figure 2.10: Example of the implementation of a $n = 4$-bit PRBS using a linear-shift feedback register [49]
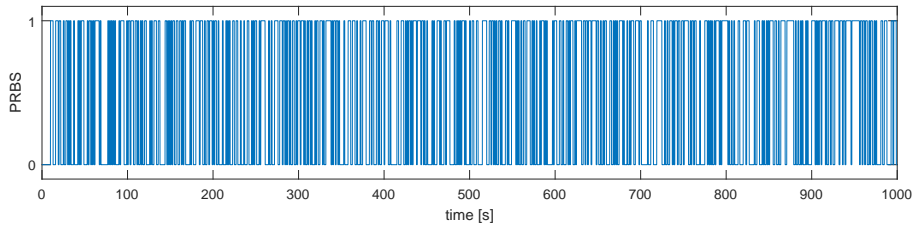
Figure 2.11: Time domain representation of 1000s of a 10-bit PRBS signal. This is the signal employed in the simulation of the Cole-Cole model response of Figure 2.14.

levels). These signals can be synthesized using linear-shift feedback registers of length n by taking the exclusive-NOR from several taps. For an n-bit shift register, the maximum sequence length of the signal is $N = 2^n - 1$. These kinds of signals have an almost flat spectrum (see Fig. 2.9) over the band of frequencies given by equation 2.5 [36]:

$$\frac{\omega_p}{N} \leq \omega \leq \frac{\omega_p}{2.3} \tag{2.5}$$

where ω is the valid frequency band, ω_p is the clock frequency of the PRBS and N is the number of periods of ω_P that are present in a single frequency. By applying this signal as an input power waveform to a thermal system and measuring the resulting temperature waveform, the system can be characterized over the frequency band. In this way, the response of the system can be determined over a range of frequencies simultaneously. In Figure 2.10 and example of the implementation of a $n = 4$-bits PRBS is shown. In 2.11 an example of the time domain of this type of signals can be observed.

2.2.5   Diffusive Representation

The Diffusive Representation (DR) was first introduced for numerical simulation of complex dynamics in [51] and extended to a general framework in [52, 53, 54]. This dynamic representation revealed to be convenient for analysis as well as modeling and control issues, but in particular, when long-memory dynamics are present (as in [55, 56, 57, 58]). Diffusive realization makes it well adapted to various problems, thanks to the nice properties of diffusion equations which allow the construction of finite-dimensional approximate state realizations simple, stable and accurate at the same time. In this Thesis, only the discretized version of the diffusive representation is presented, which can be seen as a suitable restriction of the general theory. This version is encountered in most of the bibliography where diffusive representation is used for system modeling [59, 60, 61, 62, 63]. It is known that this mathematical tool is appropiate for for approximation of fractional-order systems in practical implementations, such as thermal [62, 64, 65] or electrical [59, 66, 67] ones. This method allows the description of a physical phenomena based on diffusion using state-space models of arbitrary order.

The main interest of this modeling method for this Thesis resides in the fact that this approach

has been proven to be very suitable in thermal identification. It has been the method employed in the thermal characterization of the sensors described in 2.1.6 and 2.1.4 and explained in chapters 3 and 4. Furthermore, it has been the method employed to characterize the charge trapped in the dielectric layer of a MEMS device and described in 3.4. The theoretical grounds about diffusive reperesentation are explained below.

Diffusive representation allows obtaining exact and approximation state realizations of a wide class of integral operators [53, 68] of rational or non-rational nature. Given a non-rational transfer function, $H(p)$, associated with a convolution causal operator denoted by $H(\partial_t)$, the diffusive realization of this operator is expressed by the following input (u) – output (y) state-space realization of $u \longmapsto y = H(\partial_t)u = h * u$ of the form [59]:

$$
\begin{aligned}
\frac{\partial \psi(\xi,t)}{\partial t} &= -\xi\psi(\xi,t) + u(t), \quad \psi(\xi,0) = 0 \\
y(t) &= \int_0^\infty \eta(\xi)\psi(\xi,t)d\xi
\end{aligned}
\tag{2.6}
$$

where $\xi \in \mathbb{R}^+$ is frequency, $\eta(\xi)$ is the diffusive symbol of $H(\partial_t)$ that represents how the system behaves, and the state-variable $\psi(\xi,t)$ is a time-frequency representation of the input, called the diffusive representation of $u(t)$ [59]. In general, and in the case of linear processes, the identification under diffusive representation consists in the determination of the diffusive symbol $\eta(\xi)$, (or $\eta(\xi,t)$ if applicable), that completely characterizes the system in a state-space form. It must be noted that the non-linear case can also be approached through the extension of the theory [60]. The diffusive symbol $\eta(\xi)$ is a solution of the frequncy domain equation (2.7), which is directly obtained from Laplace transform (with respect to t) of the trasfer function $H(p)$ [59]:

$$
H(j\omega) = \int_0^\infty \frac{\eta(\xi)}{j\omega + \xi}d\xi \quad \omega \in \mathbb{R}
\tag{2.7}
$$

The impulse response $h := \mathcal{L}^{-1}H$ can also be expressed from $\eta(\xi)$ [59]:

$$
h(t) = \int_0^\infty e^{-\xi t}\eta(\xi)d\xi
\tag{2.8}
$$

and, reciprocally, the diffusive symbol can be given also as the inverse Laplace transform of the impulse response: [59]

$$
\eta = \mathcal{L}^{-1}h
\tag{2.9}
$$

It must be noted that since ξ is a continuous variable it is possible to handle infinite order systems, such as in the case of fractional operators. The complexity of equation (2.6) is intermediate between ordinary differential equations (ODE)s and partial differential (PDO)s ones. Therefore, this unified form benefits from the combination of the dynamic richness of a PDO together with the straightforward rational approximation [59].

To be able to handle experimental data, a finite-dimensional approximation, arbitrarily close to the original operator, $H(\partial_t)u$, can be built discretizing the continuous variable ξ into $\{\xi_k\}_{1 \leq k \leq K}$, where K is the finite order of the discretized model. This leads to an input – output approximation

$u \longmapsto \tilde{y} \approx H(\frac{d}{dt})u$. The discretized model can be described by:

$$\begin{array}{rcl} \frac{d\psi_k(t)}{dt} & = & -\xi_k\psi_k(t) + u(t), \quad \psi_k(0) = 0 \\ \tilde{y}(t) & = & \sum_{k=1}^{K} \eta_k\psi_k(t) \end{array} \tag{2.10}$$

where $\psi_k(t) = \psi(\xi_k, t)$ and $\eta_k = \eta(\xi_k)$ with $\eta_k \in \mathbb{R}^K$.

Figure 2.12 shows the block diagram of the discrete diffusive representation of the Laplace transform of equation (2.10).

The goodness of the approximation will depend on the chosen frequency mesh $\{\xi_k\}_{1 \leq k \leq K}$, in the band of interest and in concordance with the dynamic characteristics of the system [62]. The mesh is usually chosen so that the frequencies are geometrically spaced:

$$\xi_{k+1} = r\xi_k, \qquad r = \left(\frac{\xi_K}{\xi_1}\right)^{\left(\frac{1}{K-1}\right)} \tag{2.11}$$

This choice allows a constant quality of approximation (in terms of relative error) in each frequency decade over the whole frequency band under consideration [59]. The chosen bandwidth for ξ goes from $\xi_{min} = 2\pi/T$ to $\xi_{max} = \pi/T_s$, (in rad/s), where T is the total duration of the measurements (long enough for the stabilization of the system), and T_s is the sampling period. Therefore, the experiment duration and the sampling period set a limit on the minimum and maximum frequency, respectively. When the system under consideration is time-invariant, η_K converges, under suitable conditions, to the exact (but unknown) diffusive symbol:

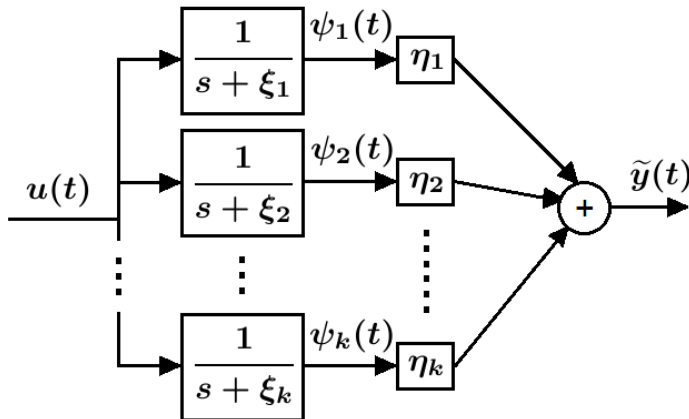$$\eta_K \xrightarrow[K\to\infty]{} \eta \tag{2.12}$$

Figure 2.12: Block diagram of the Laplace transform of the discrete diffusive representation model of (2.10)

Which means that if the frequency mesh is sufficiently dense, it is possible to describe with arbitrary accuracy the response of any fractional system.

The inference of the diffusive symbol is done from the experimental data. Considering that the measurement data is distributed in a temporal mesh, $[t_n]_{1 \le n \le N} \in \mathbb{R}^+$, we can define the matrix $\mathbf{A} = [\psi_k(t_n)]$ and the output vector of measurements as $\mathbf{Y}^T = [y(t_0), \ldots, y(t_n), \ldots, y(t_N)]$. Taking this notation into account, the solution to the identification problem is found solving the finite dimensional least squares problem formulated by [62]:

$$\min_{\eta \in \mathbb{R}^K} ||\mathbf{A}\hat{\boldsymbol{\eta}} - \mathbf{Y}||^2 \qquad (2.13)$$

that is classically solved by the standard pseudo-inversion method:

$$\hat{\boldsymbol{\eta}} = [\mathbf{A}^*\mathbf{A}]^{-1}\mathbf{A}^*\mathbf{Y} \qquad (2.14)$$

The identfication problem is often ill-conditioned because the matrix $[\mathbf{A}^*\mathbf{A}]$ is close to a non-invertible one. This problem is usually solved by adding a small penalization term $\epsilon > 0$ to the equation: [62]

$$\hat{\boldsymbol{\eta}} = [\mathbf{A}^*\mathbf{A} + \epsilon\mathbf{I}]^{-1}\mathbf{A}^*\mathbf{Y} \qquad (2.15)$$

where $\mathbf{I}$ is the identity matrix and the parameter ϵ is chosen as small as possible as long as $\hat{\eta}$ remains quasi-insesitive to important relative variations of ϵ. In practice, very small values of ϵ are sufficient to stabilize the problem.

It has to be mentioned that when resolving numerically the integral of equation (2.6), to deal with numerical approximations, standard quadrature methods have to be used. One method is based on the use of linear interpolation [59]:

$$\eta_k = \eta(\xi_k) \int_0^{+\infty} \Lambda_k(\xi)d\xi = \eta(\xi_k)\frac{\xi_{k+1} - \xi_{k-1}}{2} \qquad (2.16)$$

with Λ_k the classical interpolation function defined by:

$$\Lambda_k(\xi) = \begin{cases} 0, & \text{for } \xi \le \xi_{k-1} \text{ or } \xi \ge \xi_{k+1} \\ \frac{\xi - \xi_{k-1}}{\xi_k - \xi_{k-1}}, & \text{for } \xi_{k-1} < \xi < \xi_k \\ \frac{\xi_{k+1} - \xi}{\xi_{k+1} - \xi_k}, & \text{for } \xi_k < \xi < \xi_{k+1} \end{cases} \qquad (2.17)$$

where for $k = 1$ and $k = K$, fictious points are introduced: $\xi_0 = \xi_1/r$ and $\xi_{K+1} = r\xi_K$, being r the ratio of the geometric sequence of the mesh of ξ defined in (2.11). Regarding to the identification problems of this Thesis, to solve the integral from equation (2.6) a logarithmic change of variable has been used due to the fact that ξ variable has chosen to be spaced geometrically. Specifically, $\xi = 10^x$ and $d\xi = \ln(10)10^x dx$. Taking this into account, the second expression of equation (2.6)

becomes:

$$y(t_n) \quad = \quad \int_{x_0}^{x_1} \eta(10^x)\psi(10^x,t)\ln(10)10^x dx \approx \sum_{k=1}^{K} \eta_k \psi_k(t_n)\lambda_k \tag{2.18}$$

Therefore, the term λ_k divides the inferred diffusive symbol, $\eta_k = \frac{\hat{\eta}_k}{\lambda_k}$, where $\lambda_k = \ln(10)\log(r)\xi_k$.

For the problems proposed in the work carried out during this Thesis, we have to consider the general case where η_k is time-varying, i.e. wind changing conditions in a wind sensor. For this reason, during the research work it was necessary to reformulate the discretized approch from equation (2.10) to maintain the linearity of the model. The equations developed during the Thesis to treat the time-varying case are presented below.

$$\begin{array}{llll}
\psi_k^{(n)}(t) & = & 0 & t \in [t_0, t_n] \\
\dot{\psi}_k^{(n)}(t) & = & -\xi_k \psi_k^{(n)} + u(t) & t \in [t_n, t_{n+1}] \\
\dot{\psi}_k^{(n)}(t) & = & -\xi_k \psi_k^{(n)} & t > t_{n+1}
\end{array} \tag{2.19}$$

$$\tilde{y}(t) \quad = \quad \sum_{n,k} \eta_k^{(n)} \psi_k^{(n)}(t) + \sum_{k}^{K} c_k e^{-\xi_k(t-t_0)}$$

where $\eta_k^{(n)} \in \mathbb{R}^K$ is the diffusive symbol associated to the conditions of the system in the n-th interval in $t \in [t_n, t_{n+1}]$. In this general formulation, the state of the system at the beginning of the measurements is taken into account thanks to $c_k \in \mathbb{R}^K$ that represents the initial conditions of the system, at $t = t_0$. The time intervals are a discretization of time for which the diffusive symbols can be considered constant in a experiment. From an experiment, the discrete number of diffusive symbols that will be obtained is J. For example, in the case where a wind sensor is being characterized, J will be the number of wind velocities applied in the experiment. Each event, $\{a_j\}_{j=1,...,J}$, represents the time interval of an experiment where the diffusive symbol $\eta_k^{(n)}$ is constant.

The solution again to this identification problem is found solving the finite least squares problem from equation (2.13), but in this general case, matrix $\mathbf{A}$ is of the form shown in equation (2.20) and $\hat{\boldsymbol{\eta}}^T$ is that of equation (2.21):

$$\mathbf{A} = \begin{bmatrix} \sum_{n:g(n)=a_1} \psi_1^{(n)}(t_0) & \cdots & \sum_{n:g(n)=a_1} \psi_K^{(n)}(t_0), & \cdots & \sum_{n:g(n)=a_J} \psi_1^{(n)}(t_0) & \cdots & \sum_{n:g(n)=a_J} \psi_K^{(n)}(t_0), & [1]_k \\ \vdots & \ddots & \vdots & \vdots & \vdots & \ddots & \vdots & \vdots \\ \sum_{n:g(n)=a_1} \psi_1^{(n)}(t_F) & \cdots & \sum_{n:g(n)=a_1} \psi_K^{(n)}(t_F), & \cdots & \sum_{n:g(n)=a_J} \psi_1^{(n)}(t_F)] & \cdots & \sum_{n:g(n)=a_J} \psi_K^{(n)}(t_F), & [e^{-\xi_k(t_F-t_0)}]_k \end{bmatrix} \tag{2.20}$$

for a experiment with $t \in [t_0, t_F]$. The function $g(n)$ returns the a_j event at every n-th time interval in $t \in [t_n, t_{n+1}]_{n=0,...,N}$ at which $\eta_k^{(n)}$ is constant. Returning to the wind sensor example, $g(n)$ will return the wind applied at every interval n. In the last column of matrix (2.20), $[1]_k \in \mathbb{R}^K$ is an

all ones vector and $[e^{-\xi_k(t-t_0)}]_k = [e^{-\xi_1(t-t_0)}, \ldots, e^{-\xi_K(t-t_0)}]$. The diffusive symbol vector that is going to be inferred is of the form of equation (2.21):

$$\hat{\boldsymbol{\eta}}^T = [[\eta_1^{a_1}, \ldots, \eta_K^{a_1}]^T, \ldots, [\eta_1^{a_J}, \ldots, \eta_K^{a_J}]^T, [c_1, \ldots, c_K]^T] \qquad (2.21)$$

where $[\eta_k^{a_j}]^T$ is the diffusive symbol corresponding to the a_j event. The measurements vector, $\mathbf{Y}^T$, remains as in (2.13), and the solution to the inference problem is classically given by (2.14).

In this Thesis, the time-varying thermal dynamics models of a thermal system are extracted from open-loop measurements using diffusive representation. From a single experiment, where the thermal conditions (or events) are continuously changing (i.e. in a wind sensor, the wind speed is switched between several wind velocities) the models that represent the behaviour of the system under that conditions can be obtained. The diffusive symbols corresponding to each event, a_j (for $j = 1 \ldots J$), are inferred from a single experiment, with $t \in [t_0, t_F]$. These events are distributed in a uniformly random sequence along the experiment. Each event occurs in a time interval $t \in [t_n, t_{n+1}]_{n=0,\ldots,N}$, where N is the total number of events, such that, $N \gg J$. (For example, in a wind sensor, J will be the number of wind velocities for which the sensor will be characterized, and N will be the number of times the wind velocity has changed). All the events have a short duration $\Delta t_n = (t_{n+1} - t_n)$, where $\Delta t_n \ll t_F$, for all n. In the meantime, a PRBS heating current is applied to the heat sources of the system in open-loop, with a period $T_{PRBS} \ll \Delta t_n \ll t_F$, while the temperature of different components of the system is sensed with a period T_s. As mentioned before, in the subsection 2.2.4, PRBS signals allow to improve the quality of the fittings in presence of noise due to their wide spectrum. The frequency mesh for the time-varying case remains geometrically spaced, but in this case the minimum frequency is set according to J. Now, $\xi_{min} = (2\pi J)/T$ [in rad/s] while the maximum frequency is the same, $\xi_{max} = \pi/T_s$.

The diffusive representation framework can be generalized to the MIMO (Multiple Input/ Mulitple Output) case. In this case, the couplig between several heat sources of a system can be analyzed. Taking this into account, cross-heating models can be constructed. These models reproduce the effect of injecting a power into heat sources in parts of the structure different from the one in which the temperature is sensed. The linearity assumption of the models enables to build the thermal model by parts [62]. A detailed description of the equations governing this effect can be encountered in chapter 4.

In practice, a small value of the model order, K, is mostly sufficient to get a good aproximation. From the literature [59, 62] and the experimentality, it has been observed that low order models are enough to obtain a good fitting of the experimental data and to recover the analytical diffusive symbol. It is usually observed that increasing the model order does not improve the root mean square error between the experimental and the fitting data beyond a certain order value [67].

The main advantage of diffusive representation is that it is possible to obtain reduced order models of long-memory systems without great computational load. Besides, these state-space models are very well suited to describe the behaviour of diffusive systems under nontrivial controls, such as sliding mode controllers (see section 2.3). Therefore this has been the method employed in the characterization of the systems related to the content of this Thesis. In sections 3.1 and
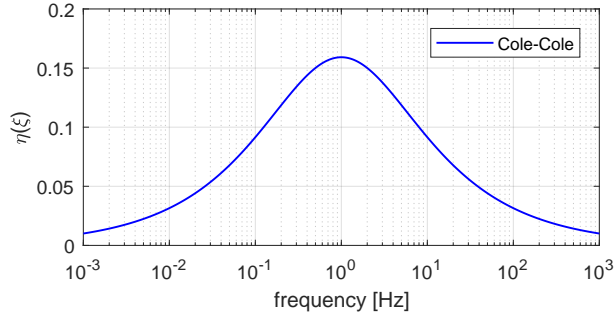
Figure 2.13: Analytical diffusive symbol of Cole-Cole dielectric model for $\alpha = 0.5$ and $\tau_0 = 1$.

3.3 the thermal dynamics of the UPC 3-D hot sphere anemometers, explained at 2.1.6, have been characterized.

2.2.6 Cole-Cole Example

As a numerical example, the Cole-Cole model is presented in this subsection. This work was necessary in the beginning of the research work, to help understand the diffusive modeling theory and to find the best input signal to obtain the best quality of the thermal system identification.

The relaxation properties of a dielectric material, as polymers, can be described in the frequency domain by the Cole-Cole equation. This model, introduced in 1941 (see [69, 70]), is still used to represent the impedance of biological tissues, to describe relaxation properties in polymers and for representing anomalous diffusion in disordered systems [71, 72, 73]. The empirical Cole-Cole
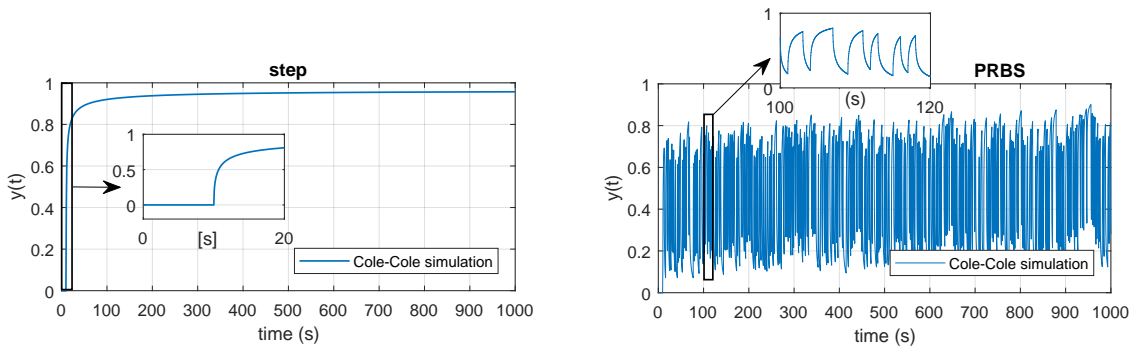
Figure 2.14: Simulation of Cole-Cole model response for $\alpha = 0.5$ and $\tau_0 = 1$. Left: Response of the model with the unitary step input signal. Right: Response of the model with a PRBS input signal.
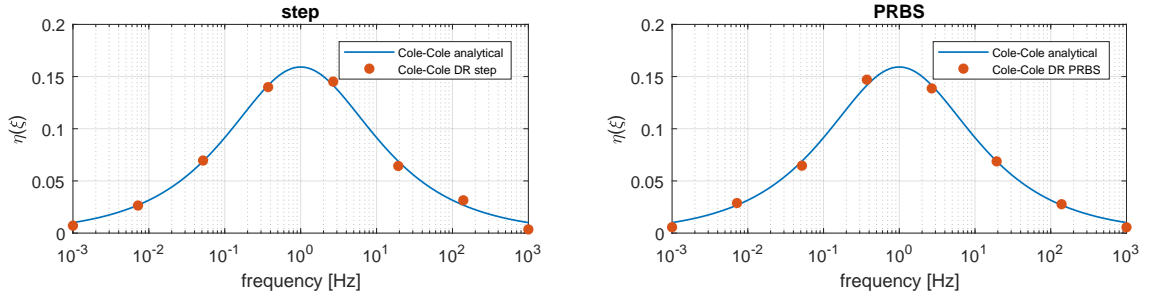
Figure 2.15: Left: Cole-Cole diffusive symbol inference for $K = 8$ when the input signal is the unitary step. Right: Cole-Cole diffusive symbol inference for $K = 8$ when the input signal is a PRBS sequence. In both cases, there is a good recovery of the diffusive symbol.

transfer function is the following:

$$H(p) \quad = \quad \frac{\varepsilon^*(p)}{(\varepsilon_s - \varepsilon_\infty)} = \frac{1}{1+(\tau_0 p)^\alpha} \tag{2.22}$$

where ε^* is the complex relative permittivity, ε_s is the static dielectric constant, ε_∞ is the high frequency dielectric constant and τ_0 is the characteristic relaxation time. The constant α allows to describe different spectral shapes and is between $0 < \alpha < 1$ [59].

The diffusive symbol associated with the Cole-Cole model is analytically computed in [59] and is given by:

$$\eta(\xi) = \frac{sin(\alpha\pi)/\pi}{(\tau_0\xi)^{-\alpha}+2cos(\alpha\pi)+(\tau_0\xi)^\alpha} \tag{2.23}$$

If we choose the value $\alpha = 0.5$, and the characteristic relaxation time is set to $\tau_0 = 1$, we have that equation (2.23) is:

$$\eta(\xi) = \frac{1}{\pi}\frac{\sqrt{\xi}}{1+\xi} \tag{2.24}$$

In Figure 2.13 the representation of the analytical Cole-Cole diffusive symbol can be observed for these given parameters.

In the following, the identification problem of the Cole-Cole system will be studied. The Cole-Cole analytical continuous function will be simulated with arbitrary inputs and will be compared with the numerical identification obtained from the diffusive representation of equation (2.10). We will see that the diffusive representation method, together with Pseudo Random Binary Sequences (PRBS), is a suitable framwework for system identification.

The output of the Cole-Cole model has been simulated from equation (2.24) for two types of input signals: the unitary step response signal and a 1Hz frequency 10-bit PRBS sequence. The simulation time has been $T = 1000$ s, with a sampling period $T_s = 5\times10^{-4}$ s. The PRBS signal employed can be observed in Figure 2.11 and in Figure 2.14 the output of the model when applying both input signals can be observed.

Figure 2.16: Left: Cole-Cole simulation data (in blue) Vs Fitting data (in red) when the input signal is the unitary step. Right: Cole-Cole simulation data (in blue) Vs Fitting data (in red) when the input signal is a PRBS sequence.
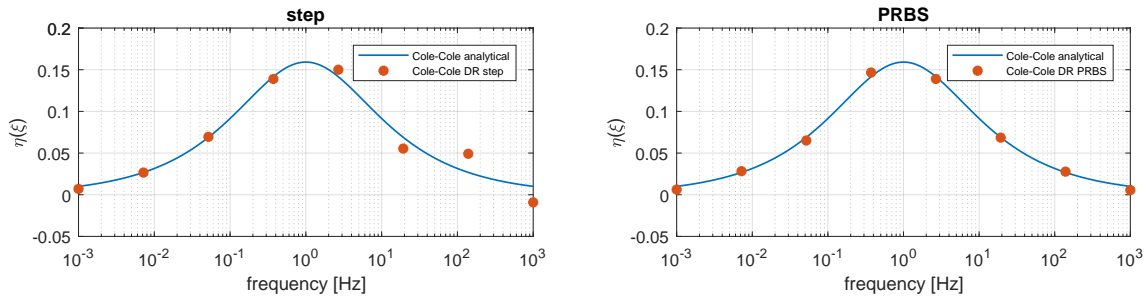
Figure 2.17: Cole-Cole diffusive symbol inference for $K = 8$ when the simulation data is added with gaussian noise. Left: when the input signal is the unitary step. Right: when the input signal is a PRBS sequence. There is a better recovery in the PRBS case.

From the simulation data of Figure 2.13 and the diffusive representation theory, the Cole-Cole diffusive symbol has been reconstructed, using the finite representation of equation (2.10). For the inference, we choose a model order of $K = 8$ and set the minimum and maximum frequencies to $f_{min} = 1/T = 1\text{x}10^{-3}$Hz and $f_{max} = 1/2T_s = 1\text{x}10^3$ Hz respectively. In Figure 2.15 we can observe that for both input signals, the unitary step and the PRBS, the diffusive symbol is well recovered with 8 poles. In both cases, the fitting of the output signal is good-matched with the simulation data (see Figure 2.16). As it can be observed, both fittings are indistinguisable from the simulation data.

At a first glance it may seem that the fact of applying a step or a PRBS signal does not make any difference in the system identification. However, it has to be noted that in the previous example the simulation data was obtained from the ideal noiseless case. If we add white gaussian noise to the simulation data, the recovery of the diffusive symbol in the case where the input signal is the unitary step does not faithfully represent the analytical case and even has one negative value. On the contrary, the recovered diffusive symbol in the case where the input signal is a PRBS sequence,
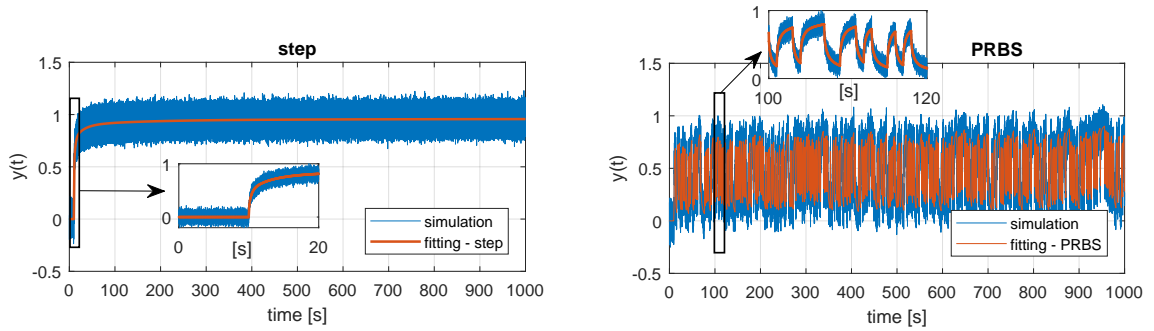
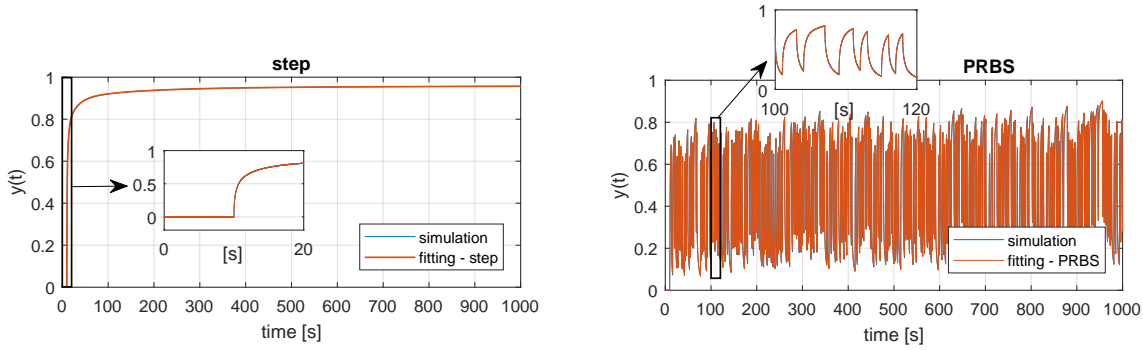**Figure 2.18:** Fitting of the Cole-Cole output when the simulation data is added with white gaussian noise. Letf: simulation data (in blue) Vs Fitting data (in red) when the input signal is the unitary step. Right: Cole-Cole simulation data (in blue) Vs Fitting data (in red) when the input signal is a PRBS sequence.

remains undisturbed. Nevertheless, in both cases (step and PRBS input signal), the fitting data has very good agreement with the noise-added simulation data. These results are observable in Figures 2.17 and 2.18.

As mentioned before, and as deduced from Figures 2.15 and 2.17, the identification is more resilient to noise when the input signal is a PRBS sequence. Moreover, when resolving the least squares problem formulated in equation (2.14), the solution is improved as the case of an ill-conditioned pseudo-inverse matrix is minimized because the input data is much more uncorrelated. For these reasons, in all the experiments carried out for system characterization of this Thesis, PRBS input signals have been employed successfully.

2.3 Sliding Mode Controllers: Sigma–Delta Modulation Approach

The Sliding Mode Control (SMC) technique is, fundamentally, a state space-based discontinuous feedback control technique. It is an efficient tool to design robust controllers for complex high-order nonlinear dynamic systems operating under uncertainty conditions [74]. The principal advantages of sliding mode control are order reduction, decoupling design procedures, disturbance rejection and their low sensitivity to systems' parameter variation, which reduces the complexity of the feedback design. This technique has been proved to be appropiate for a wide range of problems, such as robotics, process control and vehicle and motion control [74, 75, 76, 77].

In the wind sensor system presented in section 2.1.6, a closed thermal feedback loop based on thermal sigma-delta (Σ–Δ) modulation is used to keep constant the temperature in the sensor. These kinds of modulators [78] have been used for decades as analog to digital converters and also as closed-loop control circuit topologies for inertial or thermal sensors and actuators [5, 79].

With respect to the purpose of this Thesis, the thermal dynamics of the state variables of the

proposed wind sensors of section 2.1.6, under closed-loop control, have been analyzed with the tools of sliding mode controllers. It must be noted that the state variables of the thermal filter follow a sliding motion on the control surface determined by *Temperature = constant.* In this regard, no specific design of a sliding mode controller has been made, but the analysis of the resulting dynamics is made using the tools of equivalent control typical of sliding mode controllers.

2.3.1   Sigma-Delta Modulation

As it has been metioned previously, sigma-delta modulators are a class of analog to digital (A/D) converters that have been extensively studied [78]. Some of their principal advantages are the simplicity and robustness in front of component mismatch. Noise shaping and the oversampling of the input signal compensate the fact of using a very coarse quantization scheme. This allows this type of circuits to reach higher resolutions than in the case of other A/D converters, without the use of high-precision components. Besides, they can be used in the control loop of sensors or actuators to keep constant a given variable. In this way, the closed-loop control of a given variable and an implicit analog-to-digital conversion of a given magnitude are achieved [5]. One of the most used topologies is the first-order sigma-delta modulator shown in Figure 2.19

The topology of a first-order sigma-delta, takes the form of a negative feedback loop. The output of the modulator, b_n, is a digital pulse train. The output is substracted from the input to produce the error signal, which is integrated over the sampling period. The intermediate signal, u_n, is then quantized to form the output signal b_n. The main objective of the modulator is to minimize the difference between the integrated binary output and the integrated input. As a result of the feedback, the average value of the output will be a digital representation of the average value of the input signal. The equation governing the circuit of Figure 2.19 is the following:

$$u_{n+1} = u_n + \delta - sgn(u_n) \tag{2.25}$$

where δ is the magnitude to convert, $0 \leq \delta \leq 1$, assumed constant. The convention for $sgn(\rho)$ is $sgn(\rho) = 1$ for $\rho \geq 0$ and $sgn(\rho) = 0$ for $\rho < 0$. u_n is the value the integrator takes at $t = nT_s$, with T_s being the sampling period. The solution to the above equation is the following [5]:

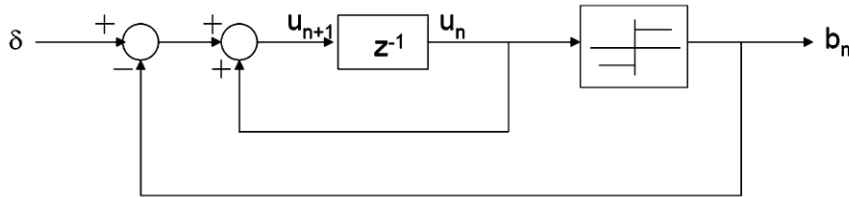$$u_n = (u_0 + (n-1)\delta)\mathrm{mod}1 - 1 + \delta \tag{2.26}$$

Figure 2.19: First-order sigma-delta modulator with constant input δ [5].

and the bitstream at the output of the modulator is

$$b_n = \delta + (u_0 + (n-1)\delta)\text{mod}1 - (u_0 + n\delta)\text{mod}1 \tag{2.27}$$

Regarding to this Thesis, the sensors presented in 2.1.6 are made to operate under constant temperature anemometry (CTA). To this effect, the temperature in the heating elements is forced to be constant. To achieve that, the implemented sigma-delta modulator applies a modulated power to the heat sources of the sensor to maintain the temperature constant. In this discrete-time control, at each sampling period, T_s, the current temperature of the structure, $T_n = T(nT_s)$, is compared with the desired target temperature, ΔT, as follows:

- If $T_n \geq \Delta T$, then the heater is switched OFF during the following sampling period (P_{off} is delivered into the heat sources).

- If $T_n < \Delta T$, then the heater is switched ON during the following sampling period (P_{on} is delivered into the heat sources).

where $P_{\text{on}} > P_{\text{off}}$. In order to be able to adapt the sensor to different flow and temperature conditions, it is usual to have a quiescent power: $P_{\text{off}} \neq 0$.

2.3.2 Sliding Mode Controllers

Sliding mode controllers are nonlinear controllers that alter the dynamics of the system by applying a discontinuous control signal so that under some conditions the system 'slides' on a certain control surface to obtain the desired behaviour of the system [80, 81]. The controller is designed in order to drive the state variables of the system into a particular surface in the state-space, named sliding surface. Once the surface is reached, sliding mode control switches from one continuous structure to another based on the current position in the state-space. Hence, sliding mode control is a variable structure control method. These types of controls alter the dynamics of a nonlinear system by application of a high frequency switching control. The discontinuous control switches from one smooth condition to another. This motion is called sliding mode. There are two main advantages in sliding mode controllers. First is that the dynamic behaviour of the system may be adapted by the particular choice of the sliding function. Secondly, the closed loop response becomes insensitive to some particular uncertainties. In the following, the dynamics of this type of control will be studied.

A dynamical model can be described as a unified state-space representation in a usual control system:

$$\dot{x} = f(x, u) \tag{2.28}$$

where $x \in \mathbb{R}^n$ is a vector which represents the state and $u \in \mathbb{R}^m$ is the control input. It is assumed that $f(\cdot)$ is differentiable with respect to x and absolutely continuous with respect to time. The

control u is a discontinuous function of the state such that:

$$u = \begin{cases} u^+(x), & \text{if } \sigma(x) > 0 \\ u^-(x), & \text{if } \sigma(x) < 0 \end{cases} \tag{2.29}$$

where we can define $\sigma = Sx(t)$, being S a surface in the state-space given by:

$$S = \{x : \sigma(x) = 0\} \tag{2.30}$$

An ideal sliding mode is said to take place on equation (2.30) if the states $x(t)$ evolve with time such that $\sigma(x(t_r)) = 0$ for some finite $t_r \in \mathbb{R}^+$ and $\sigma(x(t)) = 0$ for all $t > t_r$. The control u that drives the state variables $x(t)$ to the sliding surface of (2.30) in finite time, and keeps them on the surface thereafter, is called a sliding mode controller [82]. The main objective is to select an admissible control law u such that the control surface $\sigma(x) = 0$ is reached in a finite time.

The closed loop dynamics of a system, under the control law of (2.29) in a discrete time interval $[nT_s, (n+1)T_s]$, is given by:

$$\dot{x} = \frac{1 + sgn(\sigma(nT_s))}{2} f(x, u^+(x)) + \frac{1 - sgn(\sigma(nT_s))}{2} f(x, u^-(x)) \tag{2.31}$$

In this section, the sign function is redefined as $sgn(\rho) = +1$ when $\rho \geq 0$ and $sgn(\rho) = -1$ when $\rho < 0$. Under the infinite sampling approximation, when T_s tends to zero, the system of (2.31) can be written as a switched system [81]:

$$\dot{x} = \begin{cases} f_0(x), & \text{if } \sigma > 0 \\ f_1(x), & \text{if } \sigma < 0 \end{cases} \tag{2.32}$$

If solutions starting nearby the surface are directed towards it, the switching surface is determined as attractive, which guarantees the existance of a sliding region within the control surface. This occurs if $\sigma\dot{\sigma} < 0$, [83], with $\dot{\sigma}$ computed over the system trajectories:

$$\dot{\sigma} = S\dot{x} = \begin{cases} Sf_0(x), & \text{if } \sigma > 0 \\ Sf_1(x), & \text{if } \sigma < 0 \end{cases} \tag{2.33}$$

The attractive sliding region, or sliding domain Ω, is given by [83]:

$$\Omega := \{x \in \mathbb{R}^n : Sf_0(x) < 0\} \cap \{x \in \mathbb{R}^n : Sf_1(x) > 0\} \cap \{\sigma(x) = 0\} \tag{2.34}$$

Let us assume that the system defined in (2.32) undergoes over the switching surface with a sliding motion, i.e., the sliding domain Ω is nonempty. The obtention of the ideal sliding dynamics consists in obtaining a solution in the sense of Filippov [83]. A solution in the sense of Filippov is obtained when the system is defined on the sliding surface as a convex linear combination of $f_0(x)$

and $f_1(x)$, acting in the corresponding space region:

$$\dot{x} = (\alpha(x)f_0(x) + (1 - \alpha(x))f_1(x))\,|_{\sigma(x)=0} \tag{2.35}$$

for $\alpha(x) \in [0, 1]$. This convex combination, will be such that the derivative will be tangent to the sliding surface (see right picture of Figure 2.20). This last condition implies that the time derivative of $\sigma(x)$, evaluated at any point such that $\sigma(x) = 0$, must be zero:

$$\dot{\sigma} = 0 = S\dot{x} = (S\,(\alpha(x)f_0(x) + (1 - \alpha(x))f_1(x)))\,|_{\sigma(x)=0} \tag{2.36}$$

Taking this into account, we have that $\alpha(x) \in [0, 1]$ must be such that:

$$\alpha(x) = \left(\frac{Sf_1(x)}{Sf_1(x) - Sf_0(x)}\right)_{|_{\sigma(x)=0}} \tag{2.37}$$

The function $\alpha(x)$ may be seen as the equivalent control, u_{eq}, necessary to keep the system in the sliding surface. With this expression, the time evolution of the system once it has reached the sliding surface, this is, the sliding motion $\dot{x}$, can be described as:

$$\dot{x} = \frac{Sf_1(x)f_0(x) - Sf_0(x)f_1(x)}{Sf_1(x) - Sf_0(x)} \tag{2.38}$$

With respect to the work of this Thesis, the state-space models necessary to carry out the sliding mode analysis are provided from the diffusive representation modeling from section 2.2.5. The sliding analysis will be undertaken considering the thermal sigma-delta control explained in section 2.3.1 which is a case of a sliding mode controller. The infinite sampling frequency approximation is assumed for the obtention of the equivalent control.

In this case, under the infinite sampling approximation, the bitstream b_n, output of the sigma-delta, may be seen as a continuous time variable:

$$b_n \xrightarrow[T_s \to 0]{} b(t) = \frac{sgn(\sigma(t))}{2}\,(P_{\mathrm{on}} - P_{\mathrm{off}}) + \frac{1}{2}(P_{\mathrm{on}} + P_{\mathrm{off}}) \tag{2.39}$$

where $\sigma(t) = \Delta T - [H(\partial_t)b]\,(t)$. $H(\partial_t)$ is the convolution causal operator and was defined in section
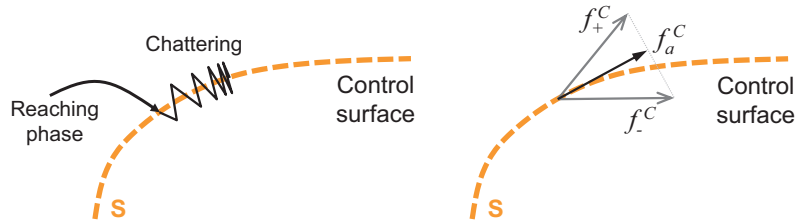

Figure 2.20: Left: Description of the sliding motion. Right: Filippov solution representation within the control surface.

2.2.5. The discretized diffusive representation model now becomes:

$$\frac{d\psi_k(t)}{dt} = \begin{cases} -\xi_k\psi_k(t) + P_{\text{on}}, & \sigma > 0 \\ -\xi_k\psi_k(t) + P_{\text{off}}, & \sigma < 0 \end{cases} \tag{2.40}$$

If we define $\Psi(t) = (\psi_1(t), \ldots, \psi_K(t)) \in \mathbb{R}^K$, the control surface can be defined as:

$$\sigma(\Psi(t)) = \Delta T - \tilde{y}(t) = \Delta T - \sum_k^K \eta_k(t)\psi_k(t) \tag{2.41}$$

for a time-varying system, and with ΔT the desired target temperature of the sigma-delta control.

A. Reachability conditions

The objective in the control is to place the system within the control surface $\sigma(\psi(t)) = 0$. In systems working at constant temperature mode, this condition is achieved when $\sum_k^K \eta_k(t)\psi_k(t) = \Delta T$. This temperature level may or may not be reached depending on the maximum and minimim heat injections, P_{on} and P_{off}. The system will reach the sliding surface $\sigma(x) = \Delta T - \sum_{k=1}^K \eta_k(t)\psi_k(t) = 0$ in finite time from any initial condition $\Psi(0)$ if:

$$P_{\text{off}} \sum_k^K \frac{\eta_k(t)}{\xi_k} < \Delta T \tag{2.42}$$

and

$$P_{\text{on}} \sum_k^K \frac{\eta_k(t)}{\xi_k} > \Delta T \tag{2.43}$$

This two conditions are achieved from the fact that the control surface $\sigma = 0$ divides in two parts the state-space. For the side of the hyperplane where $\sigma > 0$, the system evolution is:

$$\frac{d\psi_k(t)}{dt} = -\xi_k\psi_k(t) + P_{\text{on}} \tag{2.44}$$

which solution is given by:

$$\psi_k(t) = \psi_k(0)e^{-\xi_k t} + \frac{P_{\text{on}}}{\xi_k}(1 - e^{-\xi_k t}) \quad \text{for } t > 0 \tag{2.45}$$

This means that from any initial $\Psi(0)$, such that $\sigma(\Psi(0)) > 0$, the control surface $\sigma = 0$ will be reached if the asymptotic point of this trajectory lies on the other side of the hyperplane, i.e. we have condition (2.43) fullfilled. A similar analysis for $\sigma < 0$ will give us the condition of (2.42).

B. Attractive sliding region

The attractive sliding region is such that guarantees a sliding region within the control surface, under the condition $\sigma \dot{\sigma} \leq 0$. First we must note that:

$$\dot{\sigma}(\Psi(t)) = \begin{cases} \sum_k^K \eta_k(t)\xi_k\psi_k(t) - P_{\text{on}}\Gamma, & \sigma(\Psi(t)) > 0 \\ \sum_k^K \eta_k(t)\xi_k\psi_k(t) - P_{\text{off}}\Gamma, & \sigma(\Psi(t)) < 0 \end{cases} \tag{2.46}$$

where $\Gamma = \sum_k^K \eta_k(t)$. This means that the attractive sliding region is given by:

$$\Omega := \{\Psi(t) \in \mathbb{R}^K : P_{\text{off}} < \frac{1}{\Gamma} \sum_k^K \eta_k(t)\xi_k\psi_k(t) < P_{\text{on}} \cap \sigma(\Psi(t)) = 0\} \tag{2.47}$$

C. Sliding motion

The condition $\dot{\sigma}(\Psi(t)) = 0$ gives the necessary equivalent control under a sliding motion to maintain the temperature constant and for a system described by diffusive representation and considering the Filippov regularization, we have:

$$\dot{\sigma}(t) = -\sum_k^K \eta_k(t)\dot{\psi}_k(t) = \sum_k^K \eta_k(t)(\xi_k\psi_k(t) - u_{eq}(t)) = 0 \tag{2.48}$$

From this equation, the equivalent control, u_{eq}, in the sense of Filippov, is obtained:

$$u_{\text{eq}}(t) = \Gamma^{-1} \sum_k^K \eta_k(t)\xi_k\psi_k(t) \tag{2.49}$$

Then, the dynamics of the system in the control surface ($\sigma = 0$) is determined when the equivalent control is applied:

$$\dot{\psi}_k(t) + \xi_k\psi_k(t) = \Gamma^{-1} \sum_l^K \eta_l(t)\xi_l\psi_l(t) \tag{2.50}$$

If the equilibrium point ($\dot{\psi}_k(t) = 0$) is reached, the system takes the steady-state values:

$$\psi_Q(\xi_k) = \frac{u_Q}{\xi_k}$$

$$u_Q = \frac{\Delta T}{\sum_k^K \eta_k/\xi_k} \tag{2.51}$$

As mentioned before, the closed-loop dynamics of a wind sensor are being determined. Therefore, the changes in wind speed must be taken into account. The equivalent control to maintain the desired target temperature can be predicted using the diffusive symbols inferred in a previous open-loop characterization, therefore, the wind velocities for which the analysis is done must be the same as the ones for which the wind sensor has already been characterized.

The first step to calculate the equivalent control is to obtain the point $t_c \in (t_0, t_1)$ at which the system reaches the control surface, $\sigma = 0$. From a zero initial condition, a constant $u(t) = P_{on}$ is

applied till the control surface is reached. The intersection point of this initial trajectory with the surface is the initial condition for the sliding movement on the control surface following expressions (2.49) and (2.50). Now, equation (2.50) can be expressed as:

$$\dot{\psi}_k(t) = -D(t)\psi(t), \quad t \geq t_c \tag{2.52}$$

where $D(t)$ collects the terms in equation (2.50). If the wind velocities applied to the sensor are kept constant within the time intervals $\Delta t_n = (t_{n+1} - t_n)$, for $n = 0, \ldots N$, being the N time intervals of wind applied, $D(t)$ can be considered a piecewise constant and therefore for $t \in [t_n, t_{n+1}]$ we have:

$$\psi(t) = e^{-D^{(n)}(t-t_n)}\psi(t_n) \tag{2.53}$$

where:

$$D^{(n)} = \Gamma^{-1} \begin{bmatrix} \eta_1^{(n)}\xi_1 - \Gamma\xi_1 & \cdots & \eta_K^{(n)}\xi_K \\ \vdots & \ddots & \vdots \\ \eta_1^{(n)}\xi_1 & \cdots & \eta_K^{(n)}\xi_K - \Gamma\xi_K \end{bmatrix}$$

with $\eta_k^{(n)}$ the diffusive symbol of the sensor working under the wind of the n-th time interval. Replacing equation (2.53) in the equivalent control expression of equation (2.49) we reach to:

$$u_{\text{eq}}(t) = \mathbf{H}(t)\psi(t_c) \tag{2.54}$$

where:

$$\mathbf{H}(t_n) = \Gamma^{-1} \sum_k^K \eta_k(t)\xi_k e^{-D^{(n)}(t_n - t_{n-1})} e^{-D^{(n-1)}(t_{n-1} - t_{n-2})} \cdots e^{D^{(1)}(t_1 - t_c)} \tag{2.55}$$

where it has been assumed that $t_1 > t_c$.

D. Effect of external disturbances and model uncertainties

Model uncertainties and external disturbances in the system (i.e. wind velocity changes in the wind sensor) can be represented by an additional term, $\Theta(\Psi, t) = (\Theta_1(\Psi, t), \ldots, \Theta_K(\Psi, t))^T$. Since $\Psi(0) = 0$, we have that the wind sensor thermal system can be expressed as:

$$\begin{aligned} \dot{\psi}_k(t) &= -\xi_k\psi_k(t) + \tfrac{\eta_k}{2}(P_{\text{off}} + P_{\text{on}}) \\ &\quad + \tfrac{\eta_k}{2}(P_{\text{on}} - P_{\text{off}})sgn(\sigma(\Psi(t))) + \theta_k(\Psi, t) \\ \sigma(\Psi(t)) &= \Delta T - \sum_k^K \psi_k(t) \end{aligned} \tag{2.56}$$

Assuming the sliding region is taking place, this is $\dot{\sigma} = 0$, the equivalent control is now:

$$u_{eq} = \frac{\sum_k^K \xi_k\psi_k(t) - \frac{\Gamma}{2}(P_{\text{off}} + P_{\text{on}}) - \chi(\Psi, t)}{\frac{\Gamma}{2}(P_{\text{on}} - P_{\text{off}})} \in [-1, 1] \tag{2.57}$$

with $\chi(\psi, t) = \sum_k \theta_k(\psi, t)$. The new dynamics in the control surface is therefore determined by:

$$
\begin{aligned}
\dot{\psi}_k(t) &= -\xi_k \psi_k(t) + \tfrac{\eta_k}{2}(P_{\text{off}} + P_{\text{on}}) + \theta_k(\psi, t) \\
&\quad + \tfrac{\eta_k}{\Gamma}\left[\sum_l \xi_l \psi_l(t) - \tfrac{\Gamma}{2}(P_{\text{on}} + P_{\text{off}}) - \chi(\Psi, t)\right]
\end{aligned}
\tag{2.58}
$$

The disturbances can be decomposed in a matched and a mismatched component [81]. In the case of a matched disturbance, $\theta_k(t) - \frac{\eta_k}{\Gamma}\chi(\psi, t) = 0$, the disturbance is proportional to the diffusive symbol, i.e. $\theta_k(\psi, t) = \beta\eta_k$ for some $\beta \in \mathbb{R}$. Under this condition, the control method will be able to handle successfully the disturbances with a fast (almost instantaneous) response, since the dynamics of the system on the control surface would remain undisturbed. However, in the general case where a mismatched component is present, any disturbance will generate a change in the dynamics of the system on the control surface, therefore generating a slow dynamics in the equivalent control. Usually, the dynamics triggered by a mismatched component is expected to be of the same order as the one in the open-loop response, i.e., slow. One way of ensuring that any disturbance is a matched disturbance is the very simple case of having one state variable. This means that in a general case, it is very convenient to have only one significant state variable on the system.

In the literature, both tools, sliding mode controllers and diffusive representation, have been used together recently in numerical applications, as in [84] where sliding mode control laws are designed for fractional oscillators or in [85] where chaos control is given to illustrate the efficiency of the proposed method with first and second order sliding mode controllers. However, this Thesis presents a practical application, as both tools have been applied together in wind sensing thermal analysis, where it has been shown that the diffusive symbols from diffusive representation modeling of section 2.2.5 allow to predict the system behaviour under closed-loop operation control in the presence of wind variations.

2.4 Dielectric Charging in Contactless MEMS

Microelectromechanical systems (MEMS) is the technology that underlies the miniaturized mechanical and electro-mechanical elements that are made using the techniques of microfabrication. These devices are present in a great variety of applications such as communications, medicine or biotechnology. They are widely used as sensors (for sensing magnitudes such as pressure, temperature, chemical, magenetical or inertial forces) and as actuators.

For the development of this Thesis, the charge trapped in the dielectric layer of a contactless electrostatically actuated MEMS has been characterized for different voltage actuations. These devices, used as varactors, resonators or switches in a large set of applications, suffer from the undesired effect of parasitic charge trapped in the dielectric layers. The problems associated to this effect go from pull-in voltage drifts, capacitance-voltage ($C(V)$) curve shifts, to even stiction of moveable parts.

In order to study the time evolution of the trapped charge, the generic MEMS topology of

Figure 2.21, with movable-top and fixed-bottom electrodes, can be considered. The dynamics of the deflection of the upper electrode, $x(t)$, can be described by a mass-spring-damper ordinary differential equation [86]:

$$m\ddot{x}(t) + b\dot{x}(t) + kx(t) = F_{el}(x,t) \tag{2.59}$$

where m is the mass of the upper electrode, b is the damping factor, k is the spring coefficient and F_{el} is the electrostatic force applied to the movable electrode described by [86]:

$$F_{el}(t) = \frac{C(t)^2}{2A\varepsilon_0}\left(V - \frac{Q_d}{C_d}\right)^2 \tag{2.60}$$

where $C(t)$ is the total capacitance of the MEMS, Q_d is the total amount of charge trapped in the dielectric layer, ε_0 is the permitivity of the air, and $C_d = A\varepsilon_0\varepsilon_d/d$ is the capacitance of the dielectric, with ε_d the relative dielectric constant of the material, A the device area and d the dielectric layer thickness. The electrostatic force, F_{el}, is proportional to the square of the term defined as voltage shift: $V_{sh} = Q_d/C_d$, from which the net charge, Q_d, can be inferred. The $C(V)$ characteristic of the device is a function centered at this voltage, $V = V_{sh}$, and for the operation below pull-in, the $C - V$ curve can be approximated by a parabolic function [87, 88]:

$$C(V,t) = \alpha(V - V_{sh}(t))^2 + C_0 \tag{2.61}$$

where α is the second order coefficient of the parabola, fitted for each device, and C_0 is the minimum capacitance value of the curve. It must to be said that C_0 may present slow time dependances, $C_0(t)$, due to changes in temperature, humidity or in the uniformity of charge distribution [89, 90].

In order to avoid the dependance with C_0 in the $C(V)$ curve, the dynamics of the trapped charge can be obtained by measuring the capacitance of the device in two consecutive and close instants ot time t and $t + \Delta t$ at two points of the $C(V)$ curve. As a result, two capacitance values, $C^+(t)$ when $V^+ > 0$ is applied, and $C^-(t + \Delta t)$ when $V^- < 0$ is applied, are obtained. Assuming α constant and slow drifts in the charge dynamics, $V_{sh}(t) \approx V_{sh}(t + \Delta t)$ and $C_0(t) \approx C_0(t + \Delta t)$, the
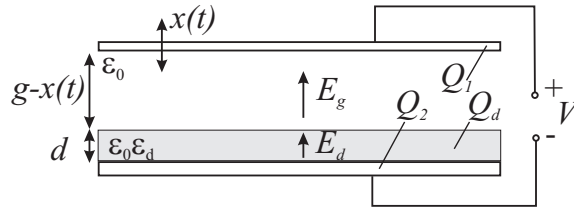

Figure 2.21: Schematic view of an electrostatic MEMS with a movable-top electrode and a dielectric layer on the fixed-bottom electrode [86].

value of V_{sh} and therefore of the dielectric charge, Q_d, is calculated from the following equation:

$$
\begin{aligned}
\Delta C(t) &= C^+(t) - C^-(t \pm \Delta t) \\
&= C(V^+(t)) - C(V^-, t \pm \Delta t) \\
&= \alpha \left((V^+)^2 - (V^-)^2 \right) - 2\alpha V_{sh}(t) \left(V^+ - V^- \right)
\end{aligned} \tag{2.62}
$$

The analysis of the charging dynamics is an important issue that has been studied using different methods and that help to the good design and operation of these systems. Therefore, measuring V_{sh} will allow us to determine the net dielectric charge in the dielectric layers of a contactless MEMS.

2.4.1 Characterization of Dielectric Charge

The effect of charging in the dielectric layer of a MEMS device occurs due to the accumulation, for a very long period of time, of charge induced by device polarization. Research in the physics behind this effect, although it is not completely understood, indicates that two are the principal processes that can contribute to external charge injection: trap-assisted tunnelling and Schottky emission from the conductor directly into the dielectric [91, 92, 93, 94, 95].

To model the long-term behaviour of the the dynamics of the trapped charge into electrostatic MEMS, different phenomenological models are usually used. The techniques employed for modeling usually analyze both charging and discharging dynamics. The charging process is analyzed by measuring the evolution of Q_d or V_{shift} while applying a specific stress voltage to a discharged device. To analyze the discharging process, after a certain time, the bias voltage is switched to $0V$. The objective of this study is to obtain a good model able to predict the charge state over time.

In the following, the more extended models to evaluate the charge evolution on a dielectric layer are presented. The total amount of net charge trapped in the dielectric layer can be expressed as $Q^n(t) + Q^p(t)$, where $Q^n(t)$ and $Q^p(t)$ are the negative and positive charges respectively. The time constants for each charge sign component are $\tau_C^{n,p}$ and $\tau_D^{n,p}$ for charge and discharge processes, respectively. This notation to express the charge accumulation has been used in [86, 96, 79, 97, 98].

Exponential dynamics modeling

The dynamics of the charge of one sign resembles an exponential function of the form $Q(t) = A_0 + A_1 e^{-(t/\tau)}$, where A_0 and A_1 are constants found from the experimental data fitting and the time constant τ represents the characteristic time scale of the process. The equations of the exponential model are the following:

$$
Q^n(t) = \begin{cases} Q_{max}^n (1 - e^{-t/\tau_C^n}) & V > 0 \\ Q_{max}^n e^{-t/\tau_D^n} & V < 0 \end{cases} \tag{2.63}
$$

$$
Q^p(t) = \begin{cases} Q_{max}^p e^{-t/\tau_D^p} & V > 0 \\ Q_{max}^p (1 - e^{-t/\tau_C^p}) & V < 0 \end{cases} \tag{2.64}
$$

where Q_{max}^p and Q_{max}^n are the saturation values of positive and negative charge, respectively. The model assumes that at the intial conditions, $t = t_0$, the charging process starts from zero $Q^{n,p}(0) = 0$ and the discharging process starts from the maximum value $Q^n(0) = Q_{max}^{n,p}$. But in the general case, there may be any arbitrary negative and positive charges accumulated in the dielectric by the time t_0: $Q_d(t_0) = Q_0 = Q^n(t_0) + Q^p(t_0), t_0 > 0$.

In [99, 100], from the experimental data, the dielectric charging of RF MEMS capacitive switches is characterized. However, this model only captures basic features, such as saturation of the charge and the time constants for charging and discharging processes.

Multi-exponential dynamics modeling

This modeling is an extension of the exponential model presented previously. The charge is characterized as a superposition of exponentials where different time constants, τ_i, are present. In this case, the dynamics of the charge resembles a multi-exponential function of the form $Q(t) = \sum_i A_i e^{-(t/\tau_i)}$. The model equations are the following:

$$Q_d^n(t) = \begin{cases} Q_{max}^n - \sum_i \zeta_i^n Q_{max}^n e^{-t/\tau_{Ci}^n} & V > 0 \\ \sum_i \zeta_i^n Q_{max}^n e^{-t/\tau_{Di}^n} & V < 0 \end{cases} \tag{2.65}$$

$$Q_d^p(t) = \begin{cases} \sum_i \zeta_i^p Q_{max}^p e^{-t/\tau_{Di}^p} & V > 0 \\ Q_{max}^p - \sum_i \zeta_i^p Q_{max}^p e^{-t/\tau_{Ci}^p} & V < 0 \end{cases} \tag{2.66}$$

where $\zeta_i^{n,p}$ specifies how the total charges are distributed along all the exponential. In this case, $Q_{max}^{n,p} = \sum_i Q_{max,i}^{n,p}$ and $\zeta_i^{n,p} = Q_{max,i}^{n,p}/Q_{max}^{n,p}$. By definition, $\sum_i \zeta_i^{n,p} = 1$.

The multi-exponential modeling has been widely used to characterize charging and discharging of traps in the dielectric layers of RF MEMS. In [101, 102, 103], the superposition model with only two time constants shows a good agreement with experimental data for different voltage actuations. In [104] an study of the reliability and the charging effect in a RF MEMS switch is carried out. Here, the experimental results are fitted and compared with one and two time constants, observing much better concordance in the two time constants case.

Stretched exponential dynamics modeling

This modeling describes the charge dynamics with one strectched exponential time constant of the form: $Q(t) = A_0 + A_1 e^{-(t/\tau)^\beta}$, where $0 < \beta < 1$. In contrast with the previous exponential and multi-exponential models, this modeling involves non-linear time t^β. It is usually described as:

$$Q_d^n(t) = \begin{cases} Q_{max}^n \left(1 - e^{-(t/\tau_C^n)^{\beta_C^n}}\right) & V > 0 \\ Q_{max}^n e^{-(t/\tau_D^n)^{\beta_D^n}} & V < 0 \end{cases} \tag{2.67}$$

$$Q_d^p(t) = \begin{cases} Q_{max}^p \left(1 - e^{-(t/\tau_C^p)^{\beta_C^p}}\right) & V > 0 \\ Q_{max}^p e^{-(t/\tau_D^p)^{\beta_D^p}} & V < 0 \end{cases} \tag{2.68}$$

In [105, 106] the charge relaxation of a silicon nitride layer is found to follow the stretched exponential law. In [89] the charging process is also described through stretched exponential relaxation law, in a RF MEMS device where the temperature dependence of the $C(V)$ characteristic is studied.

In [99] the single exponential, the stretch-exponential and the square root models are applied to fit experimental data of the charging dynamics. It has to be noted that square root of the time, $\sqrt{t}$, accurately describes the voltage shift versus time. It has to be noted also that this is also the typical response of a fractionary system. In this referenced work, a comparison among the three method is carried out, showing a best adjustment for the stretched exponential and the square root model fittings.

Diffusive Representation modeling

The dynamics of charge trapping strongly depends on the fabrication process of the device, the dielectric type, the applied voltage, and the architecture of the system (the analysis is usually linked to a specific MEMS topology) [105]. However, with diffusive representation, neither the structure or topology of the system is of relevance, as black-box state-space models of arbitrary order are obtained.

As it has been mentioned on subsection 2.2.5, diffusive representation is very useful for long-memory systems. It is know that the charge trapping in the dielectric layer of a contactless capacitive MEMS, generally, is a very slow process [91]. The use use of this type of model is appropiate since diffusion processes have been associated with dielectric charging in MEMS [107, 99]. Furthermore, there is a link in [108] between fractional systems and the typically observed multiexponential or stretched-time exponential type responses [109, 106] usually found in dielectric charging.

In this Thesis, diffusive representation has been used to obtain the dynamical models of a electrostatically actuated contactless capacitive MEMS for arbitrary excitation voltages. This method is able to reproduce the charge trapping dependence on the actuation voltage, which is typically nonlinear.

The diffusive charge characterization method has been developed from the general diffusive theory shown in subsection 2.2.5 of this Thesis. To characterize the dynamics of the charge trapped in the dielectric layer of a MEMS system, the voltage waveforms, or symbols BIT0 and BIT1, designed for charge characterization and control in [96, 79, 97, 110, 111, 98] are used. In Figure 2.22 these waveforms are shown. In BIT0, a negative voltage V^- is applied to the MEMS for a 'long' time $(1-\delta)T_s$, then a positive voltage V^+ is applied for a 'short' time T_s, being $0 < \delta < 1$, and T_s the symbol duration. In BIT1, the same timing scheme but with opposite voltages is applied. During each symbol, the capacitance of the device is measured at times $(1 - \delta)T_s$ and T_s. This allows obtaining a sample of the quasi-differential capacitance $\Delta C = C(V^+) - C(V^-)$ which is
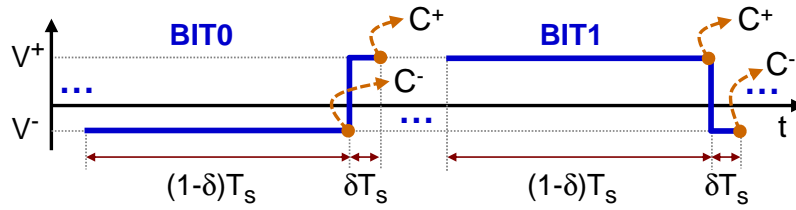
Figure 2.22: Voltage waveforms, or symbols, for MEMS actuation and sensing. Capacitance measurements are performed at symbol times $(1 - \delta)T_s$ and T_s [67].

necessary to calculate the voltage shift, V_{sh}, and therefore the charge trapped, Q_d (see equation (2.62)).

In the experimental setup, the device is actuated with BIT0 and BIT1 symbols following a specific pattern. The actuation pattern is a PRBS signal, as the ones used also for thermal system identification and explained in subsection 2.2.4. To apply the PRBS pattern, we have to combine the waveforms with each PRBS bit '0' or '1'. For each '1' or '0' of the PRBS signal, a specific number of either BIT0 or BIT1 waveforms are applied to the device. The specific number of BIT0 or BIT1 is set according the BIT0 or BIT1 duration, T_s, and the frequency of the PRBS sequence. This specific number is T_{PRBS}/T_s, where $T_{PRBS} = 1/f_{PRBS}$ is the period of the PRBS signal. As an example, lets consider a 0.01 Hz PRBS sequence (each symbol, '0' or '1' will have a duration of 100 s). If the BIT0 or BIT1 has a duration $Ts = 1$ s, for each '0' or '1' of the PRBS, 100 waveforms of BIT0 or BIT1 respectively will be applied.

Regarding to this Thesis, this has been the method employed for the charge characterization of a contactless electrostatical MEMS device, which is further explained in section 3.4.

Bibliography

[1] L. Gottesdiener. Hot wire anemometry in rarefied gas flow. *Journal of Physics E: Scientific Instruments*, 13(9):908, 1980.

[2] C. Holstein-Rathlou, J. Merrison, J. J. Iversen, A. B. Jakobsen, R. Nicolajsen, P. Nørnberg, K. Rasmussen, A. Merlone, G. Lopardo, T. Hudson, D. Banfield, and G. Portyankina. An environmental wind tunnel facility for testing meteorological sensor systems. *Journal of Atmospheric and Oceanic Technology*, 31(2):447–457, 2014.

[3] Peter A. Taylor, David C. Catling, Mike Daly, Cameron S. Dickinson, Haraldur P. Gunnlaugsson, Ari-Matti Harri, and Carlos F. Lange. Temperature, pressure, and wind instrumentation in the phoenix meteorological package. *Journal of Geophysical Research: Planets*, 113(E3), 2008. ISSN 2156-2202.

[4] Y. Zhu, B. Chen, M. Qin, and Q. A. Huang. 2-d micromachined thermal wind sensors: A review. *IEEE Internet of Things Journal*, 1(3):216–232, June 2014. ISSN 2327-4662.

[5] M. Domínguez, V. Jiménez, J. Ricart, L. Kowalski, J. Torres, S. Navarro, J. Romeral, and L. Castañer. A hot film anemometer for the martian atmosphere. *Planetary and Space Science*, 56(8):1169 – 1179, 2008. ISSN 0032-0633.

[6] T. E. Chamberlain, H. L. Cole, R. G. Dutton, G. C. Greene, and J. E. Tillman. Atmospheric measurements on mars: the viking meteorology experiment. *Bulletin of the American Meteorological Society*, 57(9):1094–1104, 1976.

[7] S. L. Hess, R. M. Henry, C. B. Leovy, J. A. Ryan, and J. E. Tillman. Meteorological results from the surface of mars: Viking 1 and 2. *Journal of Geophysical Research*, 82(28):4559–4574, 1977. ISSN 2156-2202.

[8] James R. Murphy, Conway B. Leovy, and James E. Tillman. Observations of martian surface winds at the viking lander 1 site. *Journal of Geophysical Research: Solid Earth*, 95(B9): 14555–14576, 1990. ISSN 2156-2202.

[9] NASA. Mars pathfinder web site, . URL `https://mars.nasa.gov/MPF/mpf/sci_desc.html#ATMO`.

[10] Alvin Seiff, James E. Tillman, James R. Murphy, John T. Schofield, David Crisp, Jeffrey R. Barnes, Clayton LaBaw, Colin Mahoney, John D. Mihalov, Gregory R. Wilson, and Robert Haberle. The atmosphere structure and meteorology instrument on the mars pathfinder lander. *Journal of Geophysical Research: Planets*, 102(E2):4045–4056, 1997. ISSN 2156-2202.

[11] J. T. Schofield, J. R. Barnes, D. Crisp, R. M. Haberle, S. Larsen, J. A. Magalhães, J. R. Murphy, A. Seiff, and G. Wilson. The mars pathfinder atmospheric structure investigation/meteorology (asi/met) experiment. *Science*, 278(5344):1752–1758, 1997. ISSN 00368075, 10959203.

[12] J. Gómez-Elvira, C. Armiens, L. Castañer, M. Domínguez, M. Genzer, F. Gómez, R. Haberle, A.-M. Harri, V. Jiménez, H. Kahanpää, L. Kowalski, A. Lepinette, J. Martín, J. Martínez-Frías, I. McEwan, L. Mora, J. Moreno, S. Navarro, M. A. de Pablo, V. Peinado, A. Peña, J. Polkko, M. Ramos, N. O. Renno, J. Ricart, M. Richardson, J. Rodríguez-Manfredi, J. Romeral, E. Sebastián, J. Serrano, M. de la Torre Juárez, J. Torres, F. Torrero, R. Urquí, L. Vázquez, T. Velasco, J. Verdasca, M.-P. Zorzano, and J. Martín-Torres. Rems: The environmental sensor suite for the mars science laboratory rover. *Space Science Reviews*, 170(1): 583–640, 2012. ISSN 1572-9672.

[13] S. Rafkin, J. Pla-Garcia, C. Newman, V. Hamilton, J. Martin-Torres, M. PazZorzano, H. Kahanpaa, and E. Sebastian. The meteorology of gale crater determined from msl rems data and mesoscale modeling. In *Proc. 8th Int. Conf. Mars*, pages 1–2, 2014.

[14] CAB (CSIC-INTA). Rover environmental monitoring station web site. URL `https://cab.inta-csic.es/rems/intrument-description/wind-sensor/`.

[15] NASA. Mars science laboratory web site, . URL `https://mars.nasa.gov/msl/mission/instruments/environsensors/rems/`.

[16] C. Bettanini, F. Esposito, S. Debei, C. Molfese, G. Colombatti, A. Aboudan, J. R. Brucato, F. Cortecchia, G. Di Achille, G. P. Guizzo, E. Friso, F. Ferri, L. Marty, V. Mennella, R. Molinaro, P. Schipani, S. Silvestro, R. Mugnuolo, S. Pirrotta, E. Marchetti, A. M. Harri, F. Montmessin, C. Wilson, I. A. Rodríguez, S. Abbaki, V. Apestigue, G. Bellucci, J. J. Berthelier, S. B. Calcutt, F. Forget, M. Genzer, P. Gilbert, H. Haukka, J. J. Jiménez, S. Jiménez, J. L. Josset, O. Karatekin, G. Landis, R. Lorenz, J. Martinez, D. Möhlmann, D. Moirin, E. Palomba, M. Pateli, J. P. Pommereau, C. I. Popa, S. Rafkin, P. Rannou, N. O. Renno, W. Schmidt, F. Simoes, A. Spiga, F. Valero, L. Vázquez, F. Vivat, and O. Witasse. The dreams experiment flown on the exomars 2016 mission for the study of martian environment during the dust storm season. In *2017 IEEE International Workshop on Metrology for AeroSpace (MetroAeroSpace)*, pages 249–255, June 2017.

[17] M.C. Towner, M.R. Patel, T.J. Ringrose, J.C. Zarnecki, D. Pullan, M.R. Sims, S. Haapanala, A.-M. Harri, J. Polkko, C.F. Wilson, A.P. Zent, R.C. Quinn, F.J. Grunthaner, M.H. Hecht, and J.R.C. Garry. The beagle 2 environmental sensors: science goals and instrument description. *Planetary and Space Science*, 52(13):1141 – 1156, 2004. ISSN 0032-0633.

[18] Lukasz Kowalski. *Contribution to Advanced Hot Wire Wind Sensing*. PhD thesis, Universitat Politécnica de Catalunya, 2016.

[19] L. Kowalski, M. T. Atienza, S. Gorreta, V. Jiménez, M. Domínguez-Pumar, S. Silvestre, and L. M. Castañer. Spherical wind sensor for the atmosphere of mars. *IEEE Sensors Journal*, 16(7):1887–1897, April 2016. ISSN 1530-437X.

[20] NASA. Insight mission web site, . URL `https://insight.jpl.nasa.gov/home.cfm`.

[21] NASA. Mars environmental dynamics analyzer web site, . URL `https://mars.nasa.gov/mars2020/mission/instruments/meda/`.

[22] M.N. Sabry, W. Fikry, Kh. Abdel Salam, M.M. Awad, and A.E. Nasser. A lumped transient thermal model for self-heating in mosfets. *Microelectronics Journal*, 32(10):847 – 853, 2001. ISSN 0026-2692.

[23] M. N. Sabry. Compact thermal models for electronic systems. *IEEE Transactions on Components and Packaging Technologies*, 26(1):179–185, March 2003. ISSN 1521-3331.

[24] M. Rencz and V. Szekely. Dynamic thermal multiport modeling of ic packages. *IEEE Transactions on Components and Packaging Technologies*, 24(4):596–604, Dec 2001. ISSN 1521-3331.

[25] S. Y. Lee, A. G. Pfaelzer, and J. D. van Wyk. Comparison of different designs of a 42-v/14-v dc/dc converter regarding losses and thermal aspects. *IEEE Transactions on Industry Applications*, 43(2):520–530, March 2007. ISSN 0093-9994.

[26] Guifang Guo, Bo Long, Bo Cheng, Shiqiong Zhou, Peng Xu, and Binggang Cao. Three-dimensional thermal finite element modeling of lithium-ion battery in thermal abuse application. *Journal of Power Sources*, 195(8):2393 – 2398, 2010. ISSN 0378-7753.

[27] Dong Hyup Jeon. Numerical modeling of lithium ion battery for predicting thermal behavior in a cylindrical cell. *Current Applied Physics*, 14(2):196 – 205, 2014. ISSN 1567-1739.

[28] P. L. Evans, A. Castellazzi, and C. M. Johnson. Automated fast extraction of compact thermal models for power electronic modules. *IEEE Transactions on Power Electronics*, 28 (10):4791–4802, Oct 2013. ISSN 0885-8993.

[29] S. Gao, Z. Yi, Y. Ye, Q. A. Huang, and M. Qin. Design and optimization of thermal-mechanical reliability of a tsv 3d packaged thermal wind sensor. In *2017 18th International Conference on Electronic Packaging Technology (ICEPT)*, pages 584–587, Aug 2017.

[30] Jonathan N. Davidson. *Advanced thermal modelling and management techniques to improve power density in next generation power electronics*. PhD thesis, The University of Sheffield, 2015.

[31] R. Wrobel, N. McNeill, and P. H. Mellor. Performance analysis and thermal modeling of a high-energy-density prebiased inductor. *IEEE Transactions on Industrial Electronics*, 57(1): 201–208, Jan 2010. ISSN 0278-0046.

[32] B. H. Lee, K. S. Kim, J. W. Jung, J. P. Hong, and Y. K. Kim. Temperature estimation of ipmsm using thermal equivalent circuit. *IEEE Transactions on Magnetics*, 48(11):2949–2952, Nov 2012. ISSN 0018-9464.

[33] K. Murthy and R. Bedford. Transformation between foster and cauer equivalent networks. *IEEE Transactions on Circuits and Systems*, 25(4):238–239, April 1978. ISSN 0098-4094.

[34] K. Ma, N. He, M. Liserre, and F. Blaabjerg. Frequency-domain thermal modeling and characterization of power semiconductor devices. *IEEE Transactions on Power Electronics*, 31 (10):7183–7193, Oct 2016. ISSN 0885-8993.

[35] J. N. Davidson, D. A. Stone, M. P. Foster, and C. R. Gould. Prediction of device temperatures in an electric vehicle battery charger system by analysis of device thermal cross-coupling. In *2013 15th European Conference on Power Electronics and Applications (EPE)*, pages 1–9, Sept 2013.

[36] J. N. Davidson, D. A. Stone, and M. P. Foster. Real-time prediction of power electronic device temperatures using prbs-generated frequency-domain thermal cross coupling characteristics. *IEEE Transactions on Power Electronics*, 30(6):2950–2961, June 2015. ISSN 0885-8993.

[37] X. Hu, S. Lin, S. Stanton, and W. Lian. A foster network thermal model for hev/ev battery modeling. *IEEE Transactions on Industry Applications*, 47(4):1692–1699, July 2011. ISSN 0093-9994.

[38] T. Bruckner and S. Bernet. Estimation and measurement of junction temperatures in a three-level voltage source converter. *IEEE Transactions on Power Electronics*, 22(1):3–12, Jan 2007. ISSN 0885-8993.

[39] K. Gorecki and J. Zarebski. Nonlinear compact thermal model of power semiconductor devices. *IEEE Transactions on Components and Packaging Technologies*, 33(3):643–647, Sept 2010. ISSN 1521-3331.

[40] J. N. Davidson, D. A. Stone, and M. P. Foster. Required cauer network order for modelling of thermal transfer impedance. *Electronics Letters*, 50(4):260–262, February 2014. ISSN 0013-5194.

[41] A. Bryant, N. A. Parker-Allotey, D. Hamilton, I. Swan, P. A. Mawby, T. Ueta, T. Nishijima, and K. Hamada. A fast loss and temperature simulation method for power converters, part i: Electrothermal modeling and validation. *IEEE Transactions on Power Electronics*, 27(1): 248–257, Jan 2012. ISSN 0885-8993.

[42] I. Swan, A. Bryant, P. A. Mawby, T. Ueta, T. Nishijima, and K. Hamada. A fast loss and temperature simulation method for power converters, part ii: 3-d thermal model of power module. *IEEE Transactions on Power Electronics*, 27(1):258–268, Jan 2012. ISSN 0885-8993.

[43] P. M. Igic, P. A. Mawby, M. S. Towers, and S. Batcup. New physically-based pin diode compact model for circuit modelling applications. *IEE Proceedings - Circuits, Devices and Systems*, 149(4):257–263, Aug 2002. ISSN 1350-2409.

[44] J. N. Davidson, D. A. Stone, M. P. Foster, and D. T. Gladwin. Improved bandwidth and noise resilience in thermal impedance spectroscopy by mixing prbs signals. *IEEE Transactions on Power Electronics*, 29(9):4817–4828, Sept 2014. ISSN 0885-8993.

[45] J. D. Gabano, T. Poinot, and H. Kanoun. Identification of a thermal system using continuous linear parameter-varying fractional modelling. *IET Control Theory Applications*, 5(7):889–899, May 2011. ISSN 1751-8644.

[46] W.D.T. Davies. *System Identification for Self-adaptive Control. Davies.* Wiley-Interscience, 1970.

[47] A.J. Saavedra-Montes, J.M. Ramirez-Scarpetta, C.A. Ramos-Paja, and O.P. Malik. Identification of excitation systems with the generator online. *Electric Power Systems Research*, 87 (Supplement C):1 – 9, 2012. ISSN 0378-7796.

[48] M. Singh, M. Sakare, and S. Gupta. Testing of high-speed dacs using prbs generation with alternate–bit–tapping. In *2011 Design, Automation Test in Europe*, pages 1–6, March 2011.

[49] A.J. Fairweather, M.P. Foster, and D.A. Stone. Battery parameter identification with pseudo random binary sequence excitation (prbs). *Journal of Power Sources*, 196(22):9398 – 9406, 2011. ISSN 0378-7753.

[50] J. N. Davidson, D. A. Stone, and M. P. Foster. Real-time temperature monitoring and control for power electronic systems under variable active cooling by characterisation of device thermal transfer impedance. In *7th IET International Conference on Power Electronics, Machines and Drives (PEMD 2014)*, pages 1–6, April 2014.

[51] G. Montseny, J. Audounet, and B. Mbodje. Optimal models of fractional integrators and application to systems with fading memory. In *Proceedings of IEEE Systems Man and Cybernetics Conference - SMC*, pages 65–70 vol.5, Oct 1993.

[52] Montseny, Gérard. Diffusive representation of pseudo-differential time-operators. *ESAIM: Proc.*, 5:159–175, 1998.

[53] C. Casenave and G. Montseny. Introduction to diffusive representation. *IFAC Proceedings Volumes*, 43(21):370 – 377, 2010. ISSN 1474-6670. 4th IFAC Symposium on System Structure and Control.

[54] Gerard Montseny. *Representation diffusive.* Lavoisier, 2005.

[55] Jacques Audounet, Vincent Giovangigli, and Jean-Michel Roquejoffre. A threshold phe-
nomenon in the propagation of a point source initiated flame. *Physica D: Nonlinear Phenom-
ena*, 121(3):295 – 316, 1998. ISSN 0167-2789.

[56] F. Levernhe, G. Montseny, and J. Audounet. Markovian diffusive representation of 1/f alpha;
noises and application to fractional stochastic differential models. *IEEE Transactions on
Signal Processing*, 49(2):414–423, Feb 2001. ISSN 1053-587X.

[57] David Levadoux and Gérard Montseny. *Diffusive Realization of the Impedance Operator on
Circular Boundary for 2D Wave Equation*, pages 136–141. Springer Berlin Heidelberg, Berlin,
Heidelberg, 2003. ISBN 978-3-642-55856-6.

[58] J. Solhusvik, F. Lavernhe, G. Montseny, and J. A. Farre. A new low-noise ccd signal acqui-
sition method based on a commutable band-pass filter. *IEEE Transactions on Circuits and
Systems II: Analog and Digital Signal Processing*, 44(3):164–173, Mar 1997. ISSN 1057-7130.

[59] L. Laudebat, P. Bidan, and G. Montseny. Modeling and optimal identification of pseudod-
ifferential electrical dynamics by means of diffusive representation-part i: modeling. *IEEE
Transactions on Circuits and Systems I: Regular Papers*, 51(9):1801–1813, Sept 2004. ISSN
1549-8328.

[60] Lionel Laudebat. *Modélisation et identification sous repreésentation diffusive de comporte-
ments dynamiques non rationnels en génie électrique*. PhD thesis, Universite Toulouse III -
Paul Sabatier, 2003.

[61] Emilie Blanc, Guillaume Chiavassa, and Bruno Lombard. A time-domain numerical modeling
of two-dimensional wave propagation in porous media with frequency-dependent dynamic
permeability. *The Journal of the Acoustical Society of America*, 134(6):4610–4623, 2013.

[62] B. Allard, X. Jorda, P. Bidan, A. Rumeau, H. Morel, X. Perpina, M. Vellvehi, and S. M'Rad.
Reduced-order thermal behavioral model based on diffusive representation. *IEEE Transac-
tions on Power Electronics*, 24(12):2833–2846, Dec 2009. ISSN 0885-8993.

[63] K. B. Smida, P. Bidan, T. Lebey, F. B. Ammar, and M. Elleuch. Identification and time-
domain simulation of the association inverter–cable–asynchronous machine using diffusive
representation. *IEEE Transactions on Industrial Electronics*, 56(1):257–265, Jan 2009. ISSN
0278-0046.

[64] S. M'Rad, B. Allard, H. Morel, A. Ammous, and N. Masmoudi. Analytic thermal modelling of
power electronic components: The diffusive representation. In *4th International Conference
on Integrated Power Systems*, pages 1–6, June 2006.

[65] S. Mrad, P. Lefranc, P. Dessante, P. Chiozzi, G. Blondel, M. Fakes, and P. Masson. A compact
transient electrothermal model for integrated power systems: Automotive application. In *2009
35th Annual Conference of IEEE Industrial Electronics*, pages 3755–3760, Nov 2009.

[66] C. Restrepo, G. Garcia, J. Calvente, R. Giral, and L. Martínez-Salamero. Static and dynamic current – voltage modeling of a proton exchange membrane fuel cell using an input – output diffusive approach. *IEEE Transactions on Industrial Electronics*, 63(2):1003–1015, Feb 2016. ISSN 0278-0046.

[67] M. T. Atienza, S. Gorreta, J. Pons-Nin, and M. Dominguez-Pumar. Characterization of dielectric charging in mems using diffusive representation. *IEEE Transactions on Industrial Electronics*, 64(2):1529–1533, Feb 2017. ISSN 0278-0046.

[68] G. Montseny. Simple approach to approximation and dynamical realization of pseudodifferential time operators such as fractional ones. *IEEE Transactions on Circuits and Systems II: Express Briefs*, 51(11):613–618, Nov 2004. ISSN 1549-7747.

[69] Kenneth S. Cole and Robert H. Cole. Dispersion and absorption in dielectrics i. alternating current characteristics. *The Journal of Chemical Physics*, 9(4):341–351, 1941.

[70] Kenneth S. Cole and Robert H. Cole. Dispersion and absorption in dielectrics ii. direct current characteristics. *The Journal of Chemical Physics*, 10(2):98–105, 1942.

[71] Yuri P. Kalmykov, William T. Coffey, Derrick S. F. Crothers, and Sergey V. Titov. Microscopic models for dielectric relaxation in disordered systems. *Phys. Rev. E*, 70:041103, Oct 2004.

[72] Z. Lin. On the fdtd formulations for biological tissues with cole–cole dispersion. *IEEE Microwave and Wireless Components Letters*, 20(5):244–246, May 2010. ISSN 1531-1309.

[73] B. Maundy and A. S. Elwakil. Extracting single dispersion cole–cole impedance model parameters using an integrator setup. *Analog Integrated Circuits and Signal Processing*, 71(1): 107–110, Apr 2012. ISSN 1573-1979.

[74] V. Utkin, J. Guldner, and M. Shijun. *Sliding Mode Control in Electro-mechanical Systems*. Automation and Control Engineering. Taylor & Francis, 1999. ISBN 9780748401161.

[75] Shuanghe Yu, Xinghuo Yu, Bijan Shirinzadeh, and Zhihong Man. Continuous finite-time control for robotic manipulators with terminal sliding mode. *Automatica*, 41(11):1957 – 1964, 2005. ISSN 0005-1098.

[76] Yong Feng, Xinghuo Yu, and Zhihong Man. Non-singular terminal sliding mode control of rigid manipulators. *Automatica*, 38(12):2159 – 2167, 2002. ISSN 0005-1098.

[77] Oscar Camacho and Carlos A. Smith. Sliding mode control: an approach to regulate nonlinear chemical processes. *ISA Transactions*, 39(2):205 – 218, 2000. ISSN 0019-0578.

[78] Steven R Norsworthy, Richard Schreier, Gabor C Temes, et al. *Delta-sigma data converters: theory, design, and simulation*, volume 97. IEEE press New York, 1996.

[79] S. Gorreta, J. Pons-Nin, E. Blokhina, O. Feely, and M. Domínguez-Pumar. Delta-sigma control of dielectric charge for contactless capacitive mems. *Journal of Microelectromechanical Systems*, 23(4):829–841, Aug 2014. ISSN 1057-7157.

[80] M. Dominguez-Pumar, S. Gorreta, and J. Pons-Nin. Sliding-mode analysis of the dynamics of sigma-delta controls of dielectric charging. *IEEE Transactions on Industrial Electronics*, 63(4):2320–2329, April 2016. ISSN 0278-0046.

[81] Hebertt Sira-Ramírez. *Sliding Mode Control. The Delta-Sigma Modulation Approach.* Birkhäuser Basel, 2015.

[82] Y. Shtessel, C. Edwards, L. Fridman, and A. Levant. *Sliding Mode Control and Observation.* Control Engineering. Springer New York, 2013. ISBN 9780817648930.

[83] Vadim I. Utkin. *Sliding Modes in Control and Optimization.* Springer-Verlag Berlin Heidelberg, 1992.

[84] J. Yuan and B. Shi Y. Zhang, J. Liu. Sliding mode control of vibration in single-degree-of-freedom fractional oscillators. *Journal of Dynamic Systems, Measurement, and Control*, pages 114503–114509, July 2017. ISSN 0278-0046.

[85] Maamar Bettayeb and Said Djennoune. Design of sliding mode controllers for nonlinear fractional-order systems via diffusive representation. *Nonlinear Dynamics*, 84(2):593–605, Apr 2016. ISSN 1573-269X.

[86] E. Blokhina, S. Gorreta, D. Lopez, D. Molinero, O. Feely, J. Pons-Nin, and M. Dominguez-Pumar. Dielectric charge control in electrostatic mems positioners/varactors. *Journal of Microelectromechanical Systems*, 21(3):559–573, June 2012. ISSN 1057-7157.

[87] R. W. Herfst, P. G. Steeneken, H. G. A. Huizing, and J. Schmitz. Center-shift method for the characterization of dielectric charging in rf mems capacitive switches. *IEEE Transactions on Semiconductor Manufacturing*, 21(2):148–153, May 2008. ISSN 0894-6507.

[88] R. W. Herfst, H. G. A. Huizing, P. G. Steeneken, and J. Schmitz. Characterization of dielectric charging in rf mems capacitive switches. In *2006 IEEE International Conference on Microelectronic Test Structures*, pages 133–136, March 2006.

[89] G. Papaioannou, M.N. Exarchos, V. Theonas, G. Wang, and J. Papapolymerou. Temperature study of the dielectric polarization effects of capacitive RF MEMS switches. *IEEE JMTT*, 53:3467–3473, 2005.

[90] Z. Olszewski, R. Duane, and C. O'Mahony. Effect of environment humidity on the C-V characteristics of RF MEMS capacitive switch. In *9th Int. Symp. on RF MEMS and Microsystems (MEMSWAVE)*, 29 June - 4 July 2008.

[91] S.M. Sze and K.K. Ng. *Physics of Semiconductor Devices. Third Edition.* Wiley, 2007.

[92] M. Razeghi. *Fundamentals of Solid State Engineering. Sec. Edition.* Springer, 2006.

[93] Andreas Gehring and Siegfried Selberherr. Modeling of tunneling current and gate dielectric reliability for nonvolatile memory devices. *Device and Materials Reliability, IEEE Trans. on*, 4(3):306–319, 2004.

[94] Ankit Jain, Sambit Palit, and Muhammad Ashraful Alam. A physics-based predictive modeling framework for dielectric charging and creep in RF MEMS capacitive switches and varactors. *Microelectromechanical Systems, Journal of*, 21(2):420–430, 2012.

[95] A. Koszewski, F. Souchon, Ch. Dieppedale, D. Bloch, and T. Ouisse. Physical model of dielectric charging in MEMS. *Journal of Micromechanics and Microengineering*, 23(4):045019, 2013.

[96] S. Gorreta, J. Pons-Nin, M. Dominguez-Pumar, E. Blokhina, and O. Feely. Characterization method of the dynamics of the trapped charge in contactless capacitive mems. In *2014 Symposium on Design, Test, Integration and Packaging of MEMS/MOEMS (DTIP)*, pages 1–6, April 2014.

[97] Manuel Dominguez-Pumar, Sergi Gorreta, Joan Pons-Nin, Elena Blokhina, Panagiotis Giounanlis, and Orla Feely. Real-time characterization of dielectric charging in contactless capacitive mems. *Analog Integrated Circuits and Signal Processing*, 82(3):559–569, Mar 2015. ISSN 1573-1979.

[98] Sergi Gorreta. *Dielectric charge control in contactless capacitive MEMS.* PhD thesis, Universitat Politécnica de Catalunya, 2017.

[99] R.W. Herfst, P.G. Steeneken, and J. Schmitz. Time and voltage dependence of dielectric charging in RF MEMS capacitive switches. In *IEEE 45th Annual Int. Reliability Physics Symp., Phoenix*, pages 417–421, 2007.

[100] Mohamed Matmat, Fabio Coccetti, Antoine Marty, Robert Plana, Christophe Escriba, Jean-Yves Fourniols, and Daniel Esteve. Capacitive rf mems analytical predictive reliability and lifetime characterization. *Microelectronics Reliability*, 49(9):1304 – 1308, 2009. ISSN 0026-2714. 20th European Symposium on the Reliability of Electron Devices, Failure Physics and Analysis.

[101] X. Yuan, J.C.M. Hwang, D. Forehand, and C.L. Goldsmith. Modeling and characterization of dielectric-charging effects in RF MEMS capacitive switches. In *Digest of IEEE MTT-S 2005 Microwave Symposium Digest*, pages 753–756, 2005.

[102] Xiaobin Yuan, Zhen Peng, J. C. M. Hwang, D. Forehand, and C. L. Goldsmith. A transient spice model for dielectric-charging effects in rf mems capacitive switches. *IEEE Transactions on Electron Devices*, 53(10):2640–2648, Oct 2006. ISSN 0018-9383.

[103] Z. Peng, X. Yuan, J. C. M. Hwang, D. I. Forehand, and C. L. Goldsmith. Superposition model for dielectric charging of RF MEMS capacitive switches under bipolar control-voltage waveforms. *IEEE JMTT*, 55:2911–2918, 2007.

[104] M. Matmat, K. Koukos, F. Coccetti, T. Idda, A. Marty, C. Escriba, J-Y. Fourniols, and D. Esteve. Life expectancy and characterization of capacitive RF MEMS switches. *Microelectronics Reliability*, 50:1692–1696, 2010.

[105] U. Zaghloul, G. Papaioannou, F. Coccetti, P. Pons, and R. Plana. Dielectric charging in silicon nitride films for mems capacitive switches: Effect of film thickness and deposition conditions. *Microelectronics Reliability*, 49(9):1309 – 1314, 2009. ISSN 0026-2714. 20th European Symposium on the Reliability of Electron Devices, Failure Physics and Analysis.

[106] U Zaghloul, G J Papaioannou, F Coccetti, P Pons, and R Plana. A systematic reliability investigation of the dielectric charging process in electrostatically actuated mems based on kelvin probe force microscopy. *Journal of Micromechanics and Microengineering*, 20(6): 064016, 2010.

[107] R. W. Herfst, P. G. Steeneken, J. Schmitz, A. J. G. Mank, and M. van Gils. Kelvin probe study of laterally inhomogeneous dielectric charging and charge diffusion in rf mems capacitive switches. In *2008 IEEE International Reliability Physics Symposium*, pages 492–495, April 2008.

[108] Hiroaki Hara and Yoshiyasu Tamura. Dynamical process of complex systems and fractional differential equations. *Central European Journal of Physics*, 11(10):1238–1245, 2013. ISSN 1644-3608.

[109] M. Kouteoureli and G. Papaioannou. The discharge current through the dielectric film in MEMS capacitive switches. In *European Microwave Integrated Circuits Conference (EuMIC)*, pages 450–453, Oct 2011.

[110] S. Gorreta, J. Pons-Nin, E. Blokhina, and M. Dominguez. A second-order delta-sigma control of dielectric charge for contactless capacitive mems. *Journal of Microelectromechanical Systems*, 24(2):259–261, April 2015. ISSN 1057-7157.

[111] S. Gorreta, J. Pons-Nin, and M. Dominguez-Pumar. Simultaneous control of dielectric charge and device capacitance in electrostatic mems. *Journal of Microelectromechanical Systems*, 24 (6):1684–1686, Dec 2015. ISSN 1057-7157.

Chapter 3

Compendium of Publications

This chapter describes the most important part of the research work carried out during the Thesis, in the form of a compendium of publications. The list of publications together with the abstracts is presented first, and after the complete publications in postprint format is presented.

Published:

1. **Heat Flow Dynamics in Thermal Systems Described by Diffusive Representation** on page 59.

   Abstract—The objective of this paper is to analyze the dynamics of heat flow in thermal structures working under constant temperature operation. This analysis is made using the tools of sliding mode controllers. The theory is developed considering that the thermal system can be described using diffusive representation. The experimental corroboration has been made with a prototype of a wind sensor for Mars atmosphere being controlled by a thermal sigma-delta modulator. This sensor structure allows to analyze the time-varying case experimentally since changes in wind conditions imply changes in the corresponding thermal models. The diffusive symbols of the experimental structures have been obtained from open-loop measurements in which pseudorandom binary sequences of heat are injected in the sensor. With the proposed approach, it is possible to predict heat flux transient waveforms in systems described by any arbitrary number of poles. This allows for the first time the analysis of lumped and distributed systems without any limitation on the number of poles describing it.

   http://ieeexplore.ieee.org/document/7558240/

2. **Spherical Wind Sensor for the Atmosphere of Mars** on page 69.

   Abstract—A novel wind speed and direction sensor designed for the atmosphere of Mars is described. It is based on a spherical shell divided into four triangular sectors according

to the central projection of tetrahedron onto the surface of the unit sphere. Each sector is individually controlled to be heated above the ambient temperature independently of the wind velocity and incidence angle. A convection heat rate model of four hot spherical triangles under forced wind has been built with finite element method thermal–fluidic simulations. The angular sensitivity of the tetrahedral sphere structure has been theoretically determined and compared with the tessellation of the sphere by four biangles. A 9-mm-diameter prototype has been assembled using 3-D printing of the spherical shell housing in the interior commercial platinum resistors connected to an extension of a custom design printed board. Measurements in Martianlike atmosphere demonstrate sensor responsiveness to the flow in the velocity range 1–13 m/s at 10-mBar CO_2 pressure. Numerical modelization of the sensor behavior allows to devise an inverse algorithm to retrieve the wind direction data from the raw measurements of the power delivered to each spherical sector. The functionality of the inverse algorithm is also demonstrated.

3. **Sliding mode analysis applied to improve the dynamical response of a spherical 3D wind sensor for Mars atmosphere** on page 81.

Abstract—The objective of this paper is to show how the structure of a thermal wind anemometer can be tuned to ensure a fast response when the sensor works in closed loop configuration (constant temperature operation). If the thermal filter associated to the sensor structure has only one significative time constant, the resulting system time response, working in closed loop, is enhanced beyond the natural limit imposed by its own thermal circuit. This effect is theoretically explained using the theory of sliding mode controllers. Experimental corroboration is presented by comparing the results obtained with two prototypes of a spherical wind sensor for Mars atmosphere. It will be shown that in case of having only one significant time constant, the time response in closed loop is much faster than the value associated with that time constant. It will be experimentally shown that this effect is lost when the thermal filter has more than one significant time constant. Diffusive representation is used to obtain arbitrary-order models of the thermal structures of the sensors.

4. **Characterization of Dielectric Charging in MEMS Using Diffusive Representation** on page 91.

Abstract—This paper introduces diffusive representation as a novel approach to characterize the dynamics of charge trapped in the dielectric layers of microelectromechanical systems. Diffusive representation provides a computationally efficient method to achieve an arbitrary order statespace model of the charging dynamics. This approach is particularly well suited to analyze the dynamics of the dielectric charge under nontrivial controls, as in the case of sliding mode controllers. The diffusive symbol of the experimental structure has been obtained from open-loop measurements, in which the pseudo random binary sequences are applied to the device. The obtained model exhibits good agreement with the experimental

data and also allows us to model the behavior of the charge dynamics under excitation with arbitrary binary signals.

Chapter 4

Other Thesis-related Work

This chapter includes a report of the research work done in the analysis of the thermal dynamics of the egineering model prototype of the REMS wind sensor. This work was realized in the Centro de Astrobiologia (CAB, CSIC-INTA) facilities in Madrid, during a three months stay along 2017. The results presented in this report are part of a journal paper that is actually submitted and under review. Although it is not possible to include it in the compendium of publications, it is an important part of the work developed during the research work of this Thesis.

The abstract of the submitted journal paper and the report containing a summary of the results obtained are presented.

Works:

1. **Thermal Dynamics Modeling of a 3D Wind Sensor Based on Hot Thin Film Anemometry**.

   Abstract—The objective of this paper is to obtain time-varying models of the thermal dynamics of a 3D hot thin film anemometer for Mars atmosphere. To this effect, a proof of concept prototype of the REMS wind sensor on board the Curiosity rover has been used. The self and cross-heating effects of the thermal structures have been characterized from open-loop measurements using Diffusive Representation. These models have been proven to be suitable in the analysis of the thermal dynamics of the sensor under constant temperature operation employing the tools of Sliding Mode Controllers. This analysis allows to understand the long term heat diffusion processes in the whole structure and how they may affect the raw output signals.

   Under minor revision.

DYNAMICAL THERMAL MODELS FOR THE REMS-TWINS SENSOR

M.T. Atienza, L. Kowalski, M. Domínguez-Pumar

SUMMARY

- Dynamical model of self-heating and cross-heating of the silicon dice at different wind velocities.
These models describe how the temperature of a part of the structure (a silicon die or the boom) depends on the heat dissipated in another part of the structure (in our case the silicon die).

Diffusive representation models of self-heating in the dice and heating between dice (cross-heating) have been obtained. The self-heating models depend on wind velocity and they have been made for v=0 and ±7.5m/min.

Self-heating (2.1.1): the models present significant exponentials at approximately 0.2-0.3Hz. The wind dependence can be parameterized as a variable amplitude of the pole at this frequency (higher velocity values, less amplitude).

Cross-heating (2.1.2): a model at 0 wind velocity has been obtained in which the temperature evolution of each die is calculated as a function of the heat dissipated in another die. No relevant and consistent changes have been observed at different wind velocities, for the wind velocities tested.
It has been observed symmetry in the models so that adjacent dice are heated in the same way, whereas the die in diagonal is heated differently and with much smaller amplitude.
The most significant time constant in cross-heating is at 0.1Hz.

The time evolution of the temperature in a die can be calculated as the superposition of the corresponding self-heating model and the associated cross-heating models.

- **Boom heating (2.2)**
A heating of 0.6-0.7ºC of the boom has been observed as a result of a 17ºC overheat of 4 silicon dice in one of the cards.
A DR model has been obtained describing the temperature evolution in the boom as a result of the total power injected in the four dice of one card (the same current is applied to all dice at any given moment).
Two main time constants have been found: $2x10^{-4}$ and $2x10^{-3}$ Hz (5000s and 500s respectively).

-**Prediction of the closed loop output from self-heating model (2.3.1 and 2.3.2)**
From the self-heating DR model of one die, a prediction of the output of the sigma-delta for this die, working in closed loop has been made. Wind velocity has been switched between ±7.5 m/min and 0. The analytically predicted results match the experimental results. (Figure 12).

- Comments:

- We think that an automatic control of the car in the CAB wind tunnel would be very useful.
- The influence of other heat sources (ASIC, sun radiation) on the boom temperature should be analyzed.

- Fast changes in wind temperature have not been tested.

- Appendices
Many other additional experiments can be found in the Appendix

a) Corroboration of boom heating coming from dice.
b) Dice heating coming from power dissipated in the boom resistor (!) both in open and closed-loop measurements. Boom heating generates drift in the sigma-delta output of the dice.

1. INTRODUCTION

The contents of this document are the final results obtained from the measurements done with the REMS wind sensor prototype in the wind tunnel facilities of CAB.

The boom of REMS wind sensor is composed of three PCBs placed 120º one from each other with four dice in each one. Each die has two resistors, one for heating and another for sensing, but due to practical reasons, we have only used the heating resistor both for heating and measuring the temperature.

The wind tunnel of CAB facilities is a 5-meter linear wind tunnel. The operating method consists on a car on a rail that moves to a certain velocity. Having this into account, depending of the position of the boom the signal observed at a certain velocity will be different in straight movements from position 0 to position 5m than in reverse movement from 5m to position 0m. The velocities inside the tunnel can be adjusted from 6m/min to 30m/min, that makes the car do all the way from 0 to 5m in a range from 50s to 10s, which is a very short time, taking into account the expected time constants. That is why dynamical models are needed to fully characterize the thermal response of the whole sensor system, composed of silicon dice and boom.

The boom is placed horizontally inside the tunnel. PCB1 is on top of the boom, while PCB2 and PCB3 have the normal at 120º from the top and are therefore looking downwards.

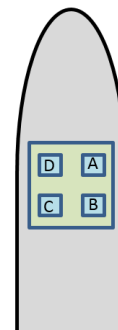Figure 1: Boom mounted inside the tunnel

Figure 2: Dice structure

In order to build finite order thermal models approximating the dynamical response of arbitrary thermal systems we have used Diffusive Representation (See Appendix 1). This mathematical tool allows generating arbitrary order models approximating experimental responses of diffusive systems, as in the case of thermal models. The main advantage of these models is that it is not necessary to make any a priori assumptions/approximations on the physical heat flows and temperature distributions of the structures and that it is possible to describe time variant systems such as the ones needed for wind sensing. Furthermore, it has been proved that with this tool it is possible to approximate even fractional order models (the ones associated typically with Partial Derivative Equations, PDEs), i.e., associated with heat diffusion on massive structures like the boom.

2. <u>EXPERIMENTAL RESULTS</u>

Different experiments have been carried out intended to obtain the diffusive representation models that help understanding the thermal dynamics of the wind sensor of REMS.

2.1. <u>AUTO AND CROSSED HEATING OF DICE</u>

Due to the proximity of the dice in the PCB, when heating one die, the rest of the dice in the PCB are affected. Therefore, when all the dice are working at the same time, the temperature of each die will depend on its self-heating current, and the current of the rest of the dice. In this section, we are going to obtain the thermal models that characterize the self-heating and cross-coupled effects. The diffusive representation equations are as follows:

<u>Auto – Heating</u>

- Heating in die A. Temperature in die A.

$$\frac{d\Psi_k^A(t)}{dt} = -\zeta_k \Psi_k^A(t) + \eta_k^{(AA)} P_A(t) \qquad \Psi_k^A(0) = 0 \qquad k = 1 \dots K$$
$$\hat{T}_A(t) = \sum_k \Psi_k^A(t)$$

- Heating in die B. Temperature in die B.

$$\frac{d\Psi_k^B(t)}{dt}(t) = -\zeta_k \Psi_k^B(t) + \eta_k^{(BB)} P_B(t) \qquad \Psi_k^B(0) = 0 \qquad k = 1 \dots K$$
$$\hat{T}_B(t) = \sum_k \Psi_k^B(t)$$

- Heating in die C. Temperature in die C.

$$\frac{d\Psi_k^C(t)}{dt} = -\zeta_k \Psi_k^C(t) + \eta_k^{(CC)} P_C(t) \qquad \Psi_k^C(0) = 0 \qquad k = 1 \dots K$$
$$\hat{T}_C(t) = \sum_k \Psi_k^C(t)$$

- Heating in die D. Temperature in die D.

$$\frac{d\Psi_k^D(t)}{dt} = -\zeta_k \Psi_k^B(t) + \mathfrak{n}_k^{(DD)} P_D(t) \qquad \Psi_k^D(0) = 0 \qquad k = 1 \dots K$$

$$\hat{T}_D(t) = \sum_k \Psi_k^D(t)$$

Where $\hat{T}_X(t)$ is the inferred temperature in die X, and $\mathfrak{n}_k^{(XX)}$ is the auto-heating diffusive symbol of die X. $\{\zeta_k\}$ is the discretized mesh of frequencies, related to the auto-heating response. As all the dice are similar among each other, we consider that the auto-heating response will be similar in all the dice, therefore we use the same frequencies and the same order K in all the dice.

Crossed-Heating

- Heating in die A. Temperature in die B,C,D.

$$\frac{d\varphi_k^A(t)}{dt} = -\rho_k \varphi_k^A(t) + P_A(t) \qquad \varphi_k^A(0) = 0 \qquad k = 1 \dots J$$

$$\hat{T}_B(t) = \sum_k \mathfrak{n}_k^{(AB)} \varphi_k^A(t)$$

$$\hat{T}_C(t) = \sum_k \mathfrak{n}_k^{(AC)} \varphi_k^A(t)$$

$$\hat{T}_D(t) = \sum_k \mathfrak{n}_k^{(AD)} \varphi_k^A(t)$$

- Heating in die B. Temperature in die A,C,D.

$$\frac{d\varphi_k^B(t)}{dt} = -\rho_k \varphi_k^B(t) + P_B(t) \qquad \varphi_k^B(0) = 0 \qquad k = 1 \dots J$$

$$\hat{T}_A(t) = \sum_k \mathfrak{n}_k^{(BA)} \varphi_k^B(t)$$

$$\hat{T}_C(t) = \sum_k \mathfrak{n}_k^{(BC)} \varphi_k^B(t)$$

$$\hat{T}_D(t) = \sum_k \mathfrak{n}_k^{(BD)} \varphi_k^B(t)$$

- Heating in die C. Temperature in die A,B,D.

$$\frac{d\varphi_k^C(t)}{dt} = -\rho_k \varphi_k^C(t) + P_C(t) \qquad \varphi_k^C(0) = 0 \qquad k = 1 \dots J$$

$$\hat{T}_A(t) = \sum_k \mathfrak{n}_k^{(CA)} \varphi_k^C(t)$$

$$\hat{T}_B(t) = \sum_k \mathfrak{n}_k^{(CB)} \varphi_k^C(t)$$

$$\hat{T}_D(t) = \sum_k \mathfrak{n}_k^{(CD)} \varphi_k^C(t)$$

- Heating in die D. Temperature in die A,B,C.

$$\frac{d\varphi_k^D(t)}{dt} = -\rho_k \varphi_k^D(t) + P_D(t) \qquad \varphi_k^D(0) = 0 \qquad k = 1 \dots J$$

$$\hat{T}_A(t) = \sum_k \mathfrak{n}_k^{(DA)} \varphi_k^D(t)$$

4 / 19

$$\hat{T}_B(t) = \sum_k \eta_k^{(DB)} \varphi_k^D(t)$$
$$\hat{T}_C(t) = \sum_k \eta_k^{(DC)} \varphi_k^D(t)$$

$\eta_k^{(YX)}$ are the diffusive symbol of the crossed effect, when applying power in die Y and inferring temperature in die X. $\{\rho_k\}$ is the discretized mesh of frequencies, related to the crossed-heating response. As all the dice are similar among each other, we consider that the crossed-heating response will be similar in all the dice, therefore we use the same frequencies and the same order J in all the dice. Note that the time response of the crossed heating effect do not have to be the same as the auto-heating effect, hence, $\{\rho_k\}$ and J can be different to $\{\zeta_k\}$ and K.

By superposition, when a power signal is injected into all the dice, A, B, C, D, the temperature inferred in each die will be:

$$\hat{T}_A(t) = \sum_k \Psi_k^A(t) + \sum_k \eta_k^{(BA)} \varphi_k^B(t) + \sum_k \eta_k^{(CA)} \varphi_k^C(t) + \sum_k \eta_k^{(DA)} \varphi_k^D(t)$$
$$\hat{T}_B(t) = \sum_k \eta_k^{(AB)} \varphi_k^A(t) + \sum_k \Psi_k^B(t) + \sum_k \eta_k^{(CB)} \varphi_k^C(t) + \sum_k \eta_k^{(DB)} \varphi_k^D(t)$$
$$\hat{T}_C(t) = \sum_k \eta_k^{(AC)} \varphi_k^A(t) + \sum_k \eta_k^{(BC)} \varphi_k^B(t) + \sum_k \Psi_k^C(t) + \sum_k \eta_k^{(DC)} \varphi_k^D(t)$$
$$\hat{T}_D(t) = \sum_k \eta_k^{(AD)} \varphi_k^A(t) + \sum_k \eta_k^{(BD)} \varphi_k^B(t) + \sum_k \eta_k^{(CD)} \varphi_k^C(t) + \sum_k \Psi_k^D(t)$$

2.1.1.   AUTO-HEATING DIFFUSIVE REPRESENTATION MODELS

The dynamical model for one die of one of the PCBs is described below. To obtain each die auto-heating diffusive symbols, four experiments have been carried out. In each experiment, a PRBS is injected in only one die, while the rest are maintained passive.

2.1.1.1. AUTO-HEATING DR MODEL FOR ZERO WIND VELOCITY

Setup:

The four experiments are identical.

- The car is stopped
- Boom position:
    - Pitch: 0º
    - Yaw: 0º
    - PCB1 is working on.

- Temperature: T amb
- Pressure = 240 mBar

- PRBS current [1- 4] mA
- PRBS frequency = 10 Hz
- Sampling frequency = 20 Hz
- Duration of experiment = 15 min

In figure 3, where the four models can be observed, there is a frequency peak at $f = 0.2\ Hz$. The model order chosen for the models auto-heating models is $K = 8$. In figure 3, the four auto-heating models can be observed. The four are very similar to each other. This is expected due to the similarity of the four dice.
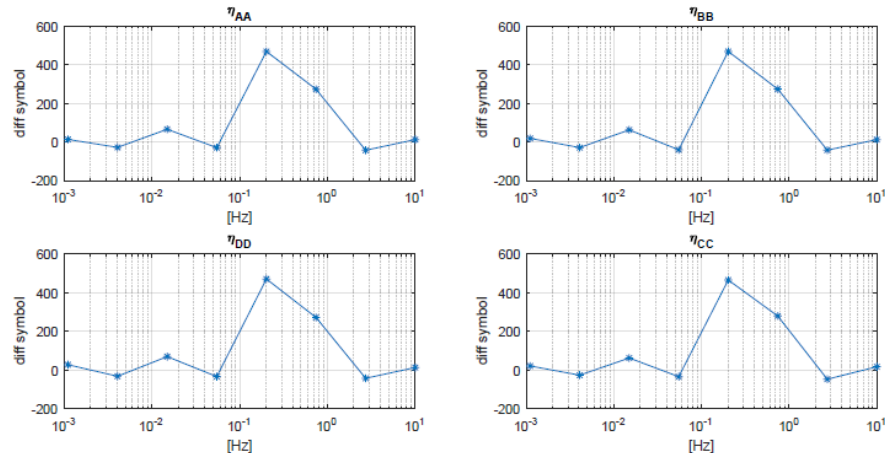

Figure 3. Auto-Heating diffusive symbols of order $K = 8$. As expected, the four auto-heating models are very similar to each order because the dice are very similar.

2.1.1.2. <u>AUTO-HEATING DR MODEL FOR V=7.5m/min WIND VELOCITY</u>

As mentioned before, velocity of the car provides two wind velocities (straight and reverse). The chosen die to infer the model from, is die B from PCB1. The election of this die has been made based on its position on the boom, Pitch = 0º / Yaw = 45º, which ensures a good wind sensitivity both in straight and reverse movement. It must be noted that, although it has good sensitivity to both movements, the response is higher in the forward direction because the incidence of the wind in the die is more direct in this case.

<u>Setup</u>:

- The car moves with a 7.5m/min velocity
- Time of the car to go from 0 to 5m and viceversa = 40s.
- Boom position:
    - Pitch: 0º
    - Yaw: 45º

- Temperature: T amb ≈ 21ºC
- Pressure ≈ 240 mBar
- Mars equivalent velocity = 2.5m/s.

- PRBS current $[1 - 4]$mA
- PRBS frequency = 20 Hz.
- Sampling frequency = 40 Hz.
- Duration of experiment ≈ 1700 s.

Figure 4 shows the velocity sequence followed by the car. Figures 5 and 6 shows the experimental results from the experiment. Three diffusive symbols are obtained from the experiment:

- v = 7.5 m/min from 0 to 5m.   (Pitch=0; Yaw=45º)
- v = - 7.5m/min from 5m to 0.   (Pitch=0; Yaw_eq = 135º)
- v = 0 m/min (stop)

As observed in figures 5 and 6, the fitting of the measurements matches well with the experimental measurements, and the three diffusive symbols are distinguishable from each other in the unique frequency peak at approximately 0.3 Hz
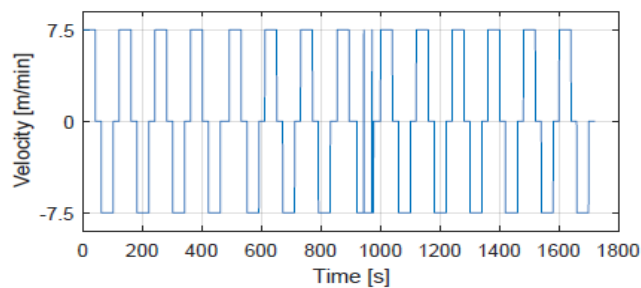
Figure 4. Velocity sequence of the car inside the tunnel in the experiment for obtaining the dynamical thermal model of a die.
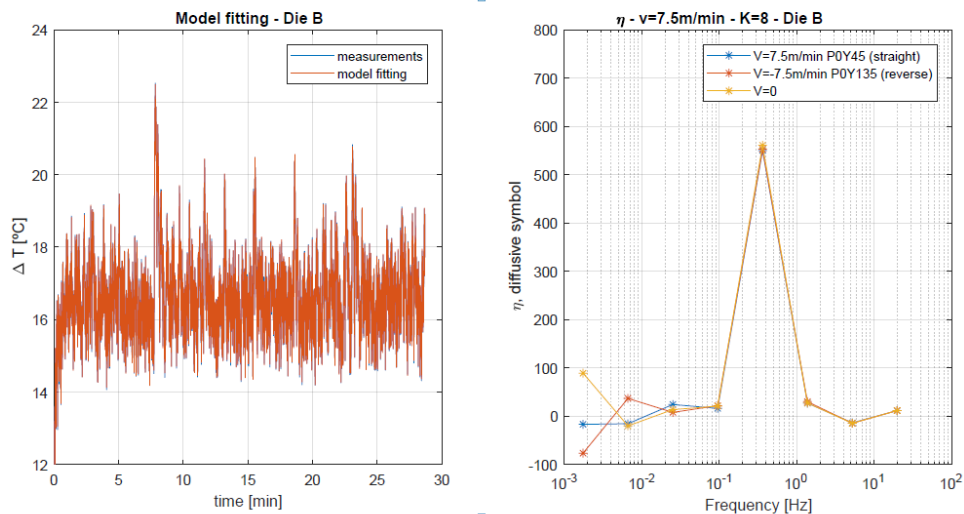
Figure 5. Left: Fitting of the temperature of die B, for car speed 7.5m/min. Rigth: 8-th order diffusive symbols, for car speed 7.5m/min
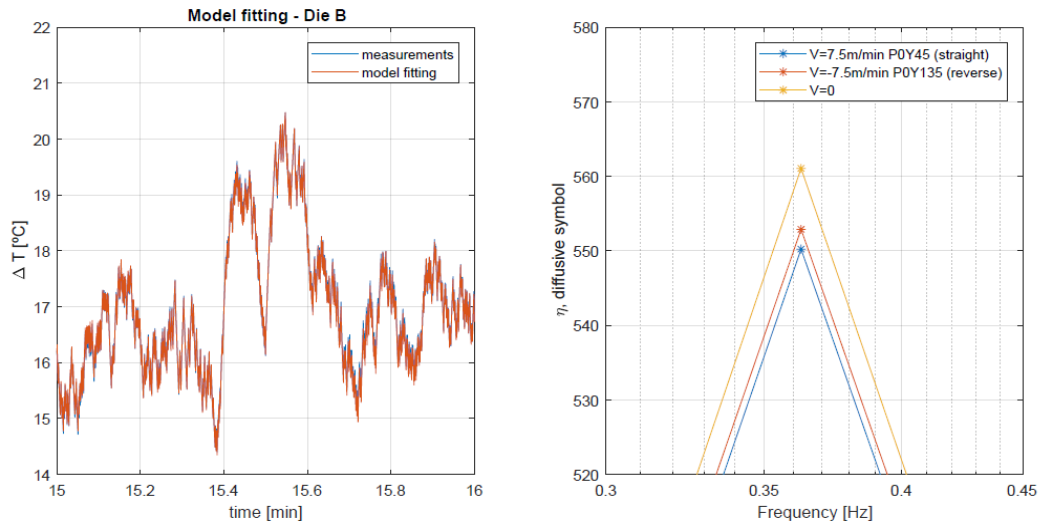
Figure 6. Left: Zoom of the fitting of the temperature of die B, for car speed 7.5m/min. Rigth: Zoom of the 8-th order diffusive symbols, for car speed 7.5m/min

2.1.2.   CROSSED-HEATING DIFFUSIVE REPRESENTATION MODELS

To obtain each die cross-heating diffusive symbols, four experiments have been carried out. In this case, in each experiment, a PRBS is injected in one of the dice, while the rest are monitored. The PRBS employed is of a lower frequency that in the case of the auto heating models, because it is known that the crossed effect has a slower response. Besides, the model is obtained at zero wind velocity because crossed models do not have dependency on wind velocity.

Setup:

The four experiments are identical.

- The car is stopped
- Boom position:
    - Pitch: 0º
    - Yaw: 0º
    - PCB1 is working on.

- Temperature: T amb
- Pressure = 240 mBar

- PRBS current [1 - 4]mA
- PRBS frequency = 1.25 Hz
- Sampling frequency = 2.5 Hz
- Duration of experiment = 1 h

In Figure 7, the crossed-heating diffusive symbols are shown. First row diffusive symbols, in blue, correspond to the effect in dice B,C,D when power is injected in die A. The second row, in red, correspond to the effect of injecting current in die B. Third row, in pink, shows the crossed

diffusive symbols of A,B, D due to heating die C. Finally, the fourth row correspond to the diffusive symbols when current is being injected in die D. As it can be observed, the model order chosen is $J = 7$, different to the model order of the auto-heating diffusive symbols. It can be observed symmetry in the diffusive symbols according to the position of the dice in the PCB. Besides, the frequency peak appears at approximately $f = 0.1\ Hz$, at a frequency smaller than the one appeared in the auto-heating components.
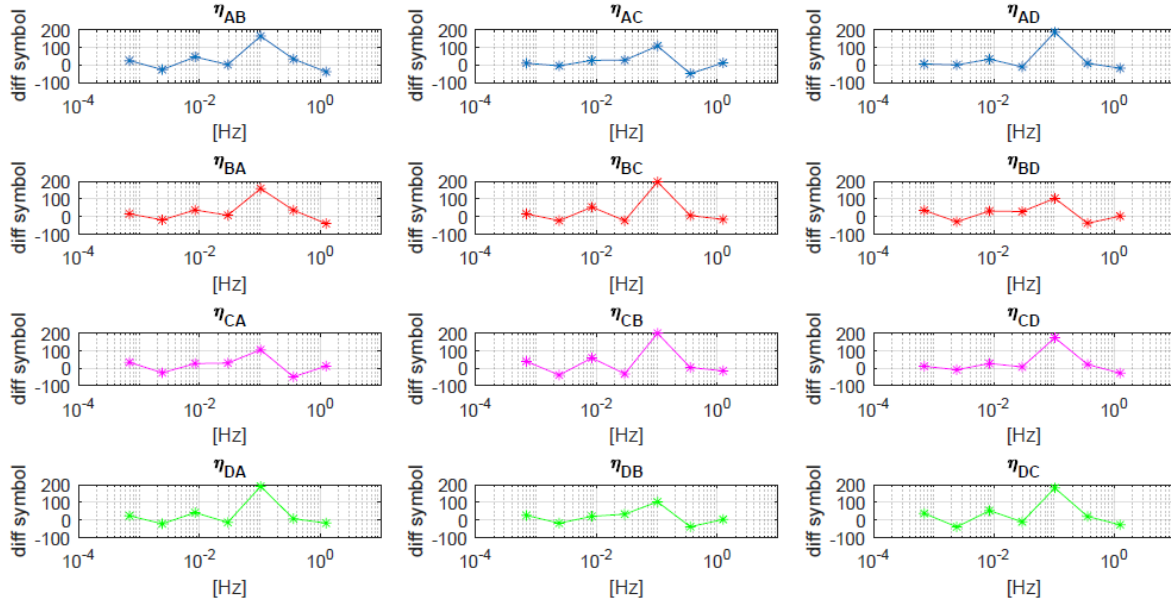
Figure 7. Cross-Heating diffusive symbols of order $J = 7$. In blue, effect in dice B,C,D when power is injected in A. In red, effect in dice A,C,D when power is injected in B. In pink, effect in A,B,D when heating die C. Finally in green, effect in A,B,C when injecting power in D. It can be observed that the crossed diffusive symbols are symmetrical due to the position of the dice in the PCB

2.2. DIFFUSIVE REPRESENTATION MODEL OF THE BOOM

From the diffusive representation theory, a model of how the boom is heated has been obtained. For this task, the input to the system is the dissipated power of all the dice when they are working under constant temperature mode and the output of the model is the temperature of the boom. We consider as input and output:

- $u(t) = P_A(t) + P_B(t) + P_C(t) + P_D(t)$
- $y(t) = T_{boom}(t) - T_{amb}(t)$

For the experiment, the temperature set on the dice is going to change randomly among three different values: 42ºC, 47ºC and 52ºC. The temperature changes every 5 minutes along the long duration experiment. As the temperature of the dice changes so it does the power.

Setup:

- The car is stopped
- Boom position:
    - Pitch: 0º
    - Yaw: 0º
    - PCB1 is working on

- Temperature: T amb (varies during the whole experiment)
- Pressure = 240 mBar
- Absolute temperature is set to 42ºC, 47ºC and 52ºC.

- Sigma-Delta currents [1-4]mA
- Sampling frequency = 1Hz
- Duration of experiment = 20h.

In figure 8, the fitting of the temperature heating of the boom together with the inferred diffusive symbol is observed. As it can be observed, there is a reasonable matching between the experimental measurements and the fitted data. The diffusive symbol peak is between $f=2x10^{-4}$ Hz and $f = 2x10^{-3}$Hz. In Figure 9, the evolution of the temperature of the dice along the 20h of the experiment is shown. Figure 10 shows the temperatures of the boom and of the sensors of the inside of the tunnel.
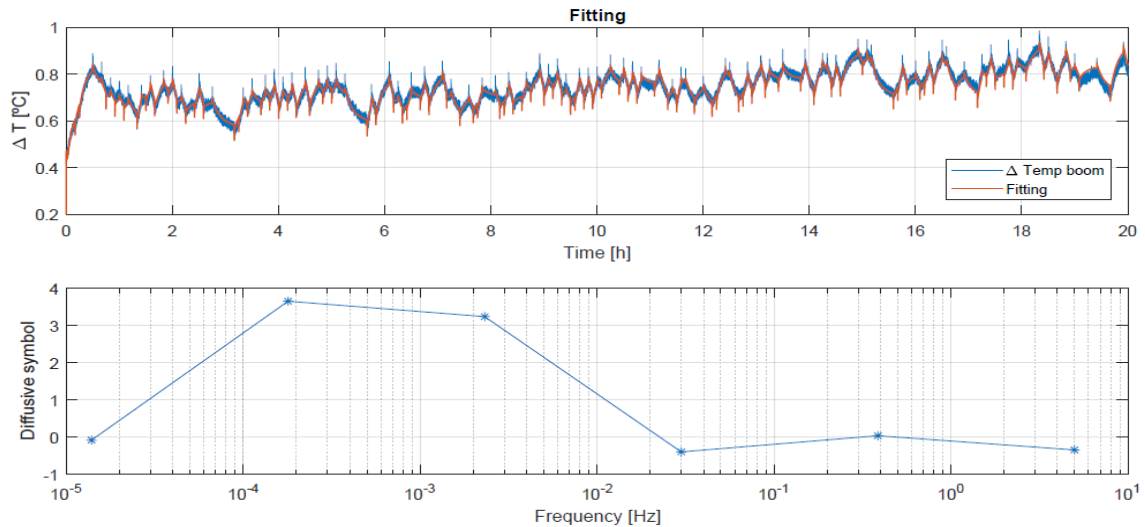

Figure 8: Top: Fitting of the difference of the temperature of the boom with the ambient temperature when a changing power is being injected in the four dice. Bottom: 6-th order diffusive symbol of the model of heating the boom
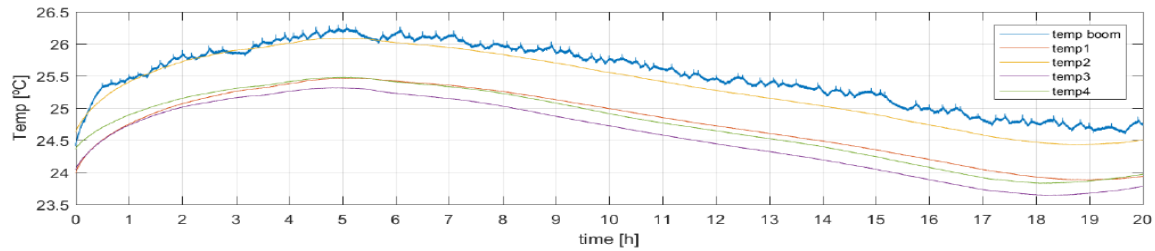
10 / 19

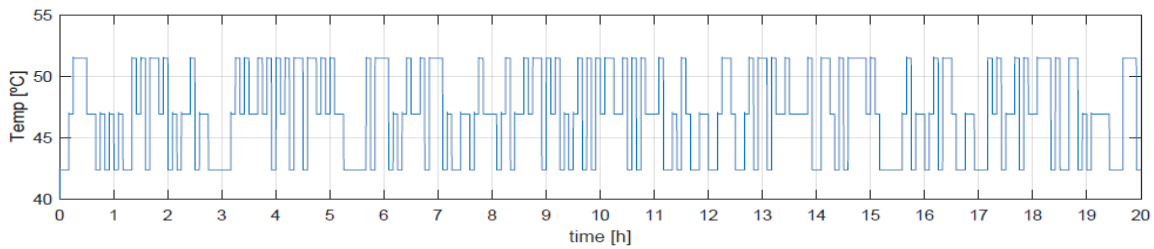Figure 9: Absolute temperatures inside the tunnel and evolution of temperature of the boom.

Figure 10: Random temperature evolution of the dice along the 20h of experiment

2.3. PREDICTION OF CLOSED LOOP POWER

With Sliding Mode Analysis theory and Diffusive Representation models obtained at section 2.1.1., it is possible to predict the closed-loop behavior under different wind velocities.

2.3.1. PREDICTION OF CLOSED-LOOP FOR ZERO WIND VELOCITY

The Diffusive Representation model for wind v=0m/min has to be obtained first. The auto-heating model from section 2.1.1.1. for the case of die B has been used. From the diffusive symbols, the equivalent control under constant temperature operation can be predicted. Figure 11 shows the results of predcting the equivalent control at zero wind velocity.

Setup:

- The car is stopped
- Boom position:
    - Pitch: 0º
    - Yaw: 0 º

- Temperature: T amb
- Pressure ≈ 240 mBar

- ΣΔ current [1 – 4]mA (Die B).
- Sampling frequency = 10 Hz.
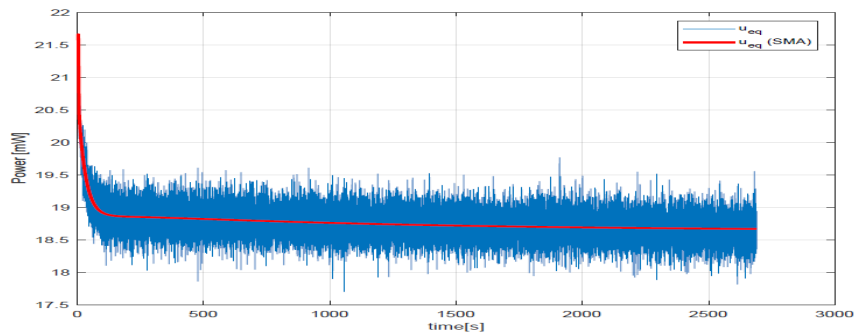- Duration of experiment ≈ 2600 s.

11 / 19

Figure 11: Prediction of equivalent control under constant temperature operation and measured equivalent control.

2.3.2.   PREDICTION OF CLOSED-LOOP FOR V=7.5 m/min WIND VELOCITY

The Diffusive Representation model for wind v=7.5m/min has to be obtained first. The auto-heating model from section 2.1.1.2. for the case of die B has been used. From the diffusive symbols, the equivalent control under constant temperature operation can be predicted. Figure 12 shows the results of predcting the equivalent control at +7.5, 0 and -7.5 wind velocities.

Setup:

-   The car is moved with a sequence: +7.5 0 -7.5 0 +7.5 0 -7.5 0
-   Boom position:
  - Pitch: 0º
  - Yaw: 45 º

-   Temperature: T amb
-   Pressure ≈ 240 mBar
-   Mars equivalent velocity = 2.5m/s.

-   ΣΔ current [1 − 4] mA (Die B. Rest Off).
-   Sampling frequency = 10 Hz.
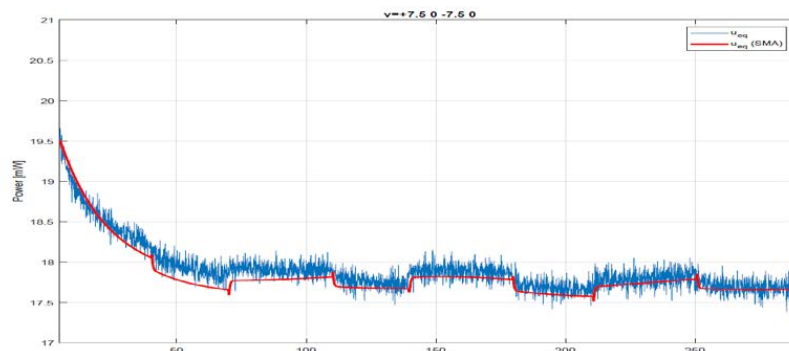-   Duration of experiment ≈ 300 s.

Figure 12: Prediction of equivalent control under constant temperature operation for several wind velocities and measured equivalent control.

3. <u>CONCLUSIONS</u>

Thermal models for the auto-heating effect for several velocities and models for the crossed – coupled effect at zero wind velocity have been obtained for the prototype of wind sensor of REMS. To achieve it, open-loop measurements have been done inside the linear tunnel of CAB facilities. From the experimental results, it has been observed that the matching between the experimental data and the data obtained from the models is good. With the diffusive representation models obtained, a prediction of the closed-loop behavior under constant temperature control has been obtained with sliding mode analysis theory.

The heating of the boom has also been demonstrated when the sensor dice are working under constant temperature mode. A model of the behavior of the heating has also been obtained with Diffusive Representation tools.

APPENDIX

    1. **HEATING OF THE BOOM**

In this experiment, we want to know if the boom is heated while the sensor is working under constant temperature mode operation. The heating of the boom is an undesired effect that may generate small drifts in the wind velocity inference when applying the inverse algorithm.

To see if the boom is heated, one of the PCBs (only one because of our system measuring limitations) is switched on and off intermittently during a long period of time. When the PCB is on, the resistors of the four dice are set to an absolute constant temperature. During the whole experiment, a Pt100 resistor of inside of the boom is measured, and the temperatures inside the tunnel are registered too.

    Setup:

- The car is stopped
- Boom position:
    - Pitch: 0º
    - Yaw: 0º
    - PCB1 is working on

- Temperature: T amb (varies during the whole experiment)
- Pressure ≈ 240 mBar
- Absolute temperature is set to 42ºC (approximately overheat of 17ºC)

- Sigma-Delta currents [1 – 4]mA
- Sampling frequency = 10 Hz.
- Duration of experiment ≈ 18h.

The tunnel has four temperature sensors inside the tunnel. Temp1 is located in the wall of the tunnel near position 0m, where the boom is located. Temp2 is located very near the boom and has a gap of 1ºC respect the rest of the temperature sensors. Temp3 and Temp4 are located in the walls of the tunnel in the middle and the end of the tunnel respectively.

The PCB is switched on and switched off in periods of 3hours. As it can be observed, in figure 22, the ambient temperature is not constant, and the general tendency of the temperature of the boom is to go with the ambient temperature. Nevertheless it is very clear that every time the PCB is switched on, there is an increase in the temperature of the boom, and when is switched off, the temperature decreases. In figure 23, it is seen that the temperature in the boom increases approximately 0.5ºC when only a PCB is working on at an overheat respect ambient temperature of 17ºC.
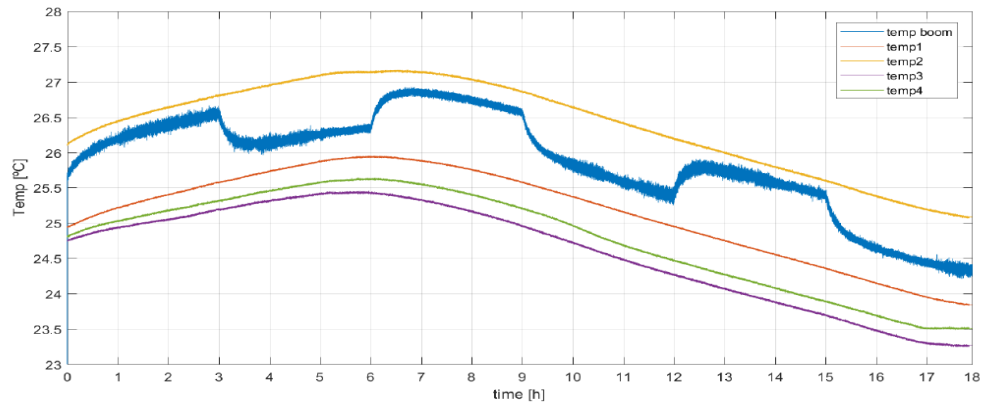
Figure 22. Temperatures evolution during the experiment. In the temperature of the boom, the moments when the PCB is on and off can be observed.
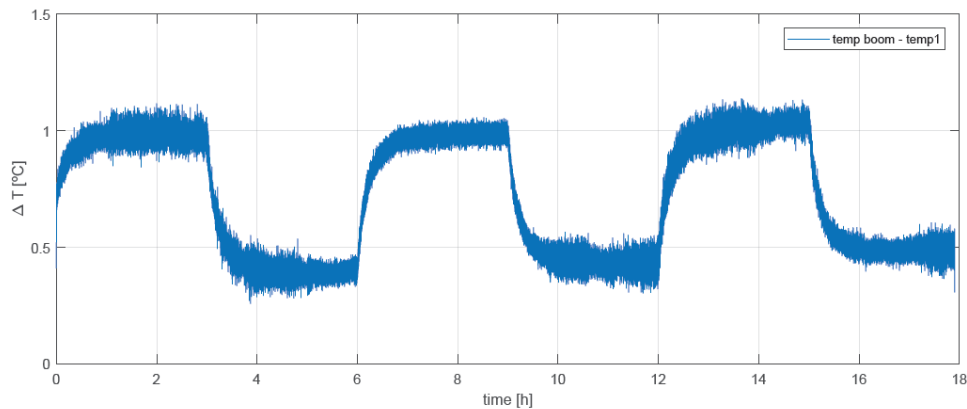

Figure 23. Temperatures difference between boom temperature and ambient temperature along the experiment. An overheat of 0.5ºC is observed in the boom when only one PCB is working at 17ºC overheat

2.   HEATING OF THE DICE

Analogously as in section 1, where the boom was heated when the dice are on, the dice of the PCB are heated by the effect of heating the boom, as expected. For the experiment, the Pt100 of the boom is set to a constant temperature, while the resistances of the four dice of a PCB are measured. The boom Pt100 is switched on and off in intervals of 2 hours.

 Setup:

- The car is stopped
- Boom position:
    o   Pitch: 0º
    o   Yaw: 0º

15 / 19

　　　　o   PCB1 dice are monitorized

-   Temperature: T amb (varies during the whole experiment)
-   Pressure = 240 mBar
-   Absolute temperature in boom is set to 28.5ºC (111 Ω)

-   Sigma-Delta currents in boom [10 - 19.9]mA
-   Sampling frequency = 10Hz
-   Duration of experiment = 8h.

The dice are heated when the boom boom closed loop control is switched on and are cooled when it is off. When the boom control is off, the dice are expected to be all at the same tunel air temperature.
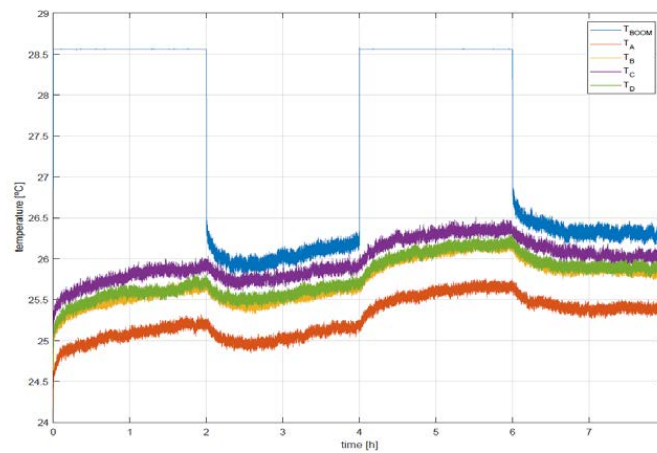

Figure 24. Temperature of the boom and the dice along the experiment. A heating in the dice is observed when heating the boom.
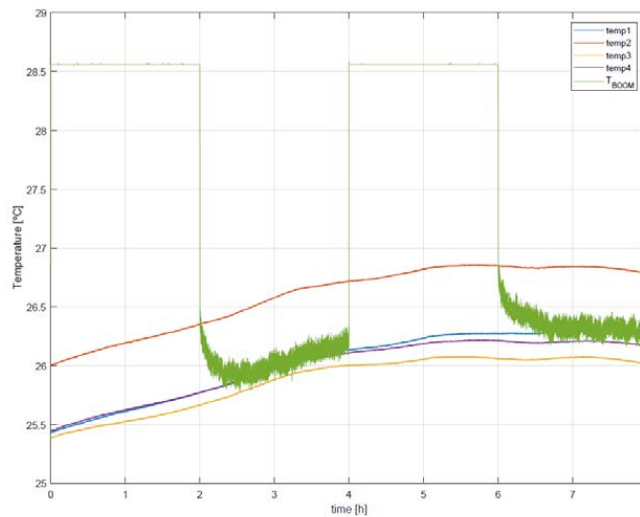

Figure 25. Temperatures inside the tunnel and that of the boom during the experiment.

16 / 19

3. DRIFT IN DICE POWER AS AN EFFECT OF HEATING OF BOOM

The effect of heating the boom in the dissipated power in the dice want to be observed. For this purpose, a slow PRBS sequence of current is injected into the Pt100 attached to the boom while the dice are set to a constant temperature (closed-loop).

Setup:

- The car is stopped
- Boom position:
    - Pitch: 0º
    - Yaw: 0º
    - PCB1 is working on

- Temperature: T amb
- Pressure = 240 mBar
- Absolute temperature set in the dice ≈ 40ºC

- Sigma-Delta currents in the dice [1 - 4] mA
- PRBS current in the boom [8.9 - 19.9]mA
- PRBS frequency = 0.0083 Hz   (2 min period)
- Sampling frequency = 10Hz
- Duration of experiment = 1h.

In figure 26 the temperature of the Pt100 of the boom and that of the dice is observed. Figure 27, the effect of the heating of the boom in the Σ-Δ power can be observed. The ambient temperature is constantly increasing, therefore the power should be decreasing constantly in consequence. But as it can be observed there are power increments/decrements related to the moments when the current changes in the boom.
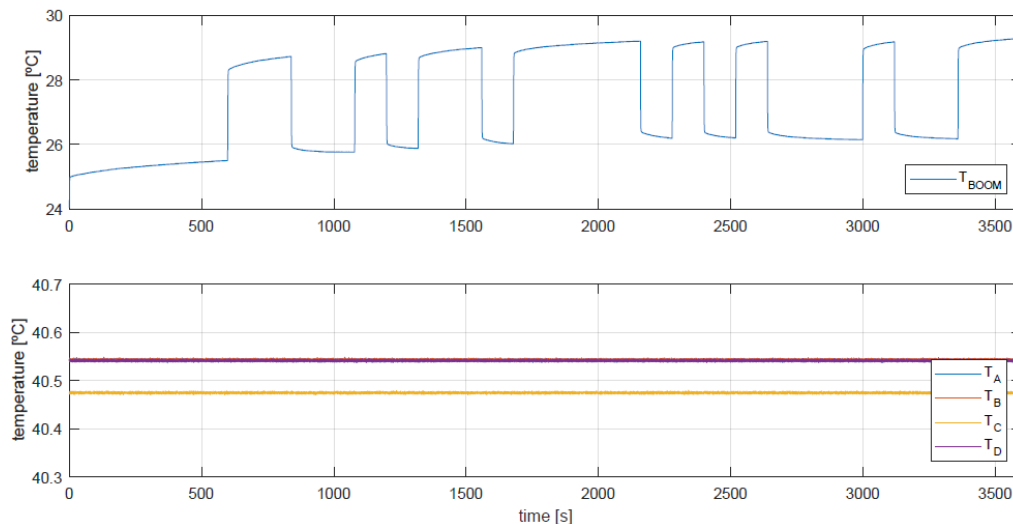

Figure 26. Top: Temperature of the boom when a slow PRBS current is being injected. Bottom: Temperature of the dice (constant) under constant temperature control
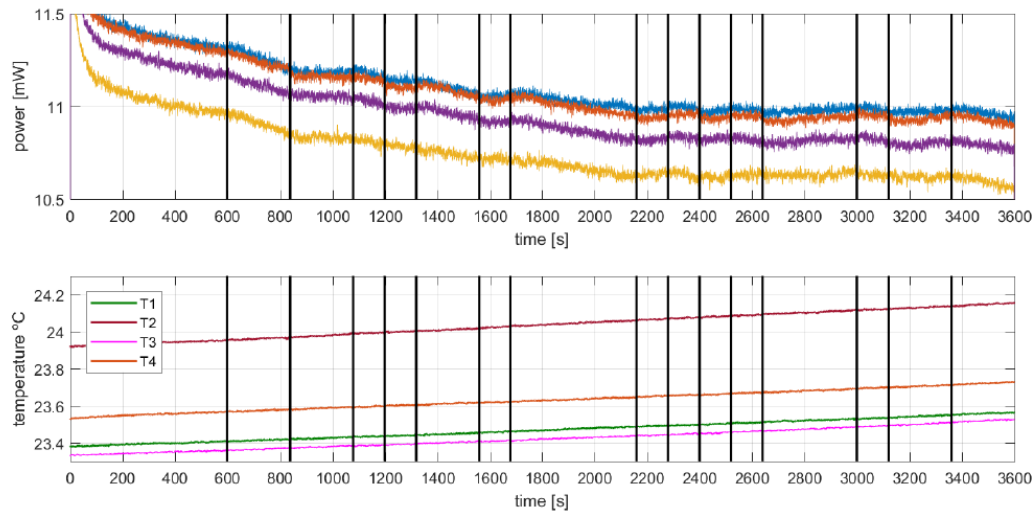
17 / 19

Figure 27. Top. Power dissipated in the dice when working under constant temperature and instants when the PRBS current of the boom changes. Increments and decrements related to the PRBS current changes can be observed.. Bottom. Increasing temperatures inside the tunel along the experiment

4.   PREDICTION OF THE TEMPERATURE IN THE DICE

Having in advance the cross-coupled and auto-heating models, it is possible to predict the temperature at each die when all the dice are working simultaneously, applying superposition as explained in section 3.5.

In the experiment, four PRBS current sequences have been injected into the four dice, to validate the models obtained previously in sections 3.5.1 and 3.5.2.

Setup:
- The car is stopped
- Boom position:
     o Pitch: 0º
     o Yaw: 0º
     o PCB1 is working on.

- Temperature: T amb
- Pressure = 240 mBar

- PRBS current in four dice simultaneously [1 - 4]mA
- PRBS frequency = 10 Hz
- Sampling frequency = 20 Hz
- Duration of experiment = 1 h

As it can be observed in Figures 28 and 29, the prediction matches relatively good to the experimental measurements. As it can be observed in Figure 31 the crossed-heating effect contributes to the temperature of a die 10 ºC
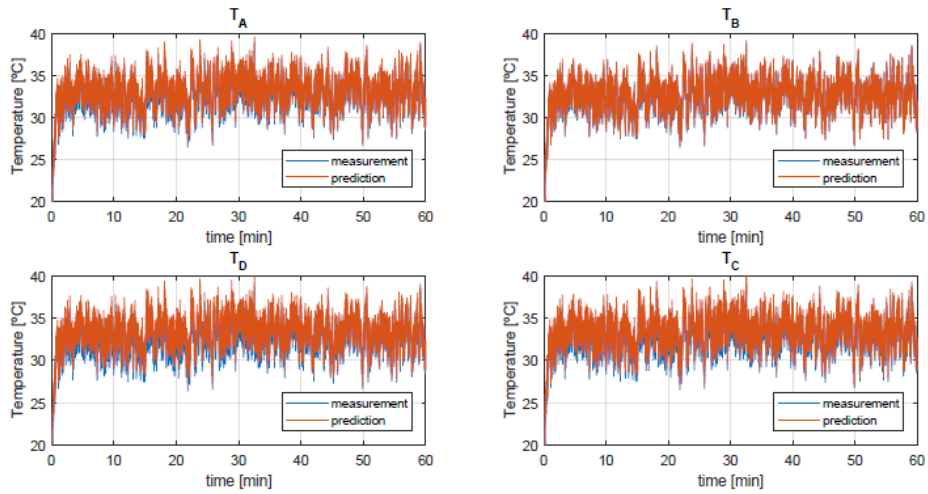

Figure 28: Prediction of the temperature at each die, applying superposition of the auto-heating and the crossed-heating effects. It can be observed a good matching between the measurement and the prediction
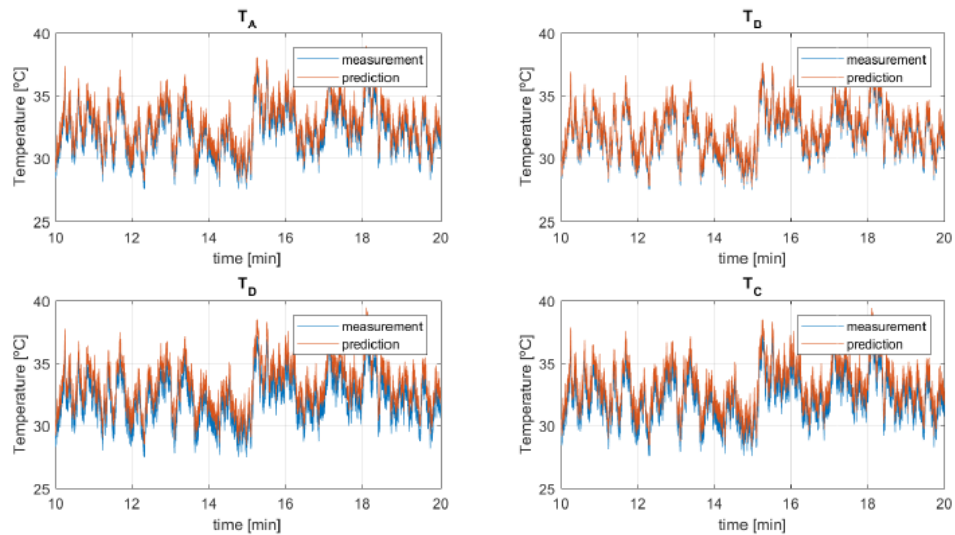

Figure 29: Zoom of 10 minutes of the prediction of the temperature at each die, applying superposition of the auto-heating and the crossed-heating effects.

Chapter 5

Conclusions and Future Work

5.1 Conclusions

The goal of this Thesis was to contribute to the analysis and modeling of diffusive systems. More specifically, to find the models that describe the thermal dynamics of different wind sensors based on thermal anemometry and to characterize the charge trapped in the dielectric layer of a capacitive MEMS.

   The main conclusions of the research work can be summarized as follows:

- The time-varying thermal dynamics models of different prototypes of a 3-dimensional spherical wind sensor based on thermal anemometry have been obtained for different wind velocities, using the tools of Diffusive Representation.

- The closed-loop dynamics under constant temperature operation has been predicted for various prototypes of a 3-dimensional spherical wind sensor. The prediction was performed for different wind velocities and using the Sliding Mode Controllers theory.

- The thermal dynamics response of two different 3-dimensional spherical wind sensors has been compared and studied. With the sliding mode analysis, it has been experimentally proven that the reduction to only one significant time constant in a system will lead to a faster time response under-closed loop, where the control will almost instantaneously absorb the changes due to external variations.

- The time-varying thermal dynamics models of the engineering model prototype of the REMS wind sensor have been obtained. The thermal cross-coupling models between differents parts of the structure of the aforementioned sensor have been experimentally obtained.

- An analysis of the self-heating and cross-heating effects of the engineering model prototype of the REMS wind sensor has been done. It has been seen that the heating of the supporting structure of the sensor may influence in the normal operation of the wind sensor.

- The charge trapped in the dielectric layer of a contactless capacitive MEMS has been characterized for different voltage actuations using the tools of Diffusive Representation.

As a result of this Thesis, four top ranked peer reviewed journal papers have been published.

5.2   Future Work

The contributions of this Thesis can be seen as a first step towards the analysis of other kind of devices.

Concerning thermal systems:

- Extend the thermal dynamics characterization method used in the engineering model of the REMS wind sensor to the engineering model of the MEDA (Mars Dynamical Environmental Analyzer) wind sensor. The MEDA wind sensor, similar in design to the REMS wind sensor, will have a more complex structure, where the thermal cross-coupling effects could affect to a greater extent.

Concerning to dielectric charge:

- Application of the diffusive representation modeling to other devices suffering from dielectric charge related effects, such as MOS structures.

Appendices

Appendix A

Conferences and Workshops

This appendix contains the Conference and Workshops where some of the main subjects of the research work of this Thesis have been presented.

<div style="border: 1px solid black; background: grey;">

ATTENTION¡¡

For copyright reasons publications must be consulted on the publisher's website indicated in the grey box

</div>

Works:

1. **Improvement of the Dynamical Response Of a Spherical 3D Wind Sensor for Mars Atmosphere** on page 125.

   Presented in *14th International Planetary Probe Workshop*, in The Hague, The Netherlands, Jun, 2017.

   https://pub-lib.jpl.nasa.gov/docushare/dsweb/View/Collection-1152

2. **Time-Varying Thermal Dynamics Modeling of the Prototype of the REMS Wind Sensor** on page 127.

   Presented in *31th European Space Thermal Analysis Workshop*, in Noordwijk, The Netherlands, Oct. 2017.

   https://exchange.esa.int/thermal-workshop/workshop2017/

3. **Sliding mode control of heterogeneous systems** on page 129.

   Presented in *Springer Special Issue of Research Perspectives CRM Barcelona: Nonsmooth Dynamics*, in Barcelona, Spain, Feb. 2016.

   https://link.springer.com/chapter/10.1007/978-3-319-55642-0_9